



Universiteit
Leiden
The Netherlands

Invasive margin tissue-resident macrophages of high CD163 expression impede responses to T cell-based immunotherapy

Elsas, M.J. van; Labrie, C.; Etzerodt, A.; Charoentong, P.; Thans, J.J.C.V.; Hall, T. van; Burg, S.H. van der

Citation

Elsas, M. J. van, Labrie, C., Etzerodt, A., Charoentong, P., Thans, J. J. C. V., Hall, T. van, & Burg, S. H. van der. (2023). Invasive margin tissue-resident macrophages of high CD163 expression impede responses to T cell-based immunotherapy. *Journal For Immunotherapy Of Cancer*, 11(3). doi:10.1136/jitc-2022-006433





Version: Publisher's Version

License: [Creative Commons CC BY-NC 4.0 license](https://creativecommons.org/licenses/by-nc/4.0/)

Downloaded from: <https://hdl.handle.net/1887/3641602>

Note: To cite this publication please use the final published version (if applicable).

Invasive margin tissue-resident macrophages of high CD163 expression impede responses to T cell-based immunotherapy

Marit J van Elsas ¹, Camilla Labrie,¹ Anders Etzerodt ², Pornpimol Charoentong,³ Jordi J C van Stigt Thans,¹ Thorbald Van Hall ¹, Sjoerd H van der Burg ¹

To cite: van Elsas MJ, Labrie C, Etzerodt A, *et al.* Invasive margin tissue-resident macrophages of high CD163 expression impede responses to T cell-based immunotherapy. *Journal for ImmunoTherapy of Cancer* 2023;**11**:e006433. doi:10.1136/jitc-2022-006433

► Additional supplemental material is published online only. To view, please visit the journal online (<http://dx.doi.org/10.1136/jitc-2022-006433>).

Accepted 21 February 2023



© Author(s) (or their employer(s)) 2023. Re-use permitted under CC BY-NC. No commercial re-use. See rights and permissions. Published by BMJ.

¹Department of Medical Oncology, Onco Institute, Leiden University Medical Center, Leiden, The Netherlands

²Department of Biomedicine, Aarhus University, Aarhus, Denmark

³Department of Medical Oncology, National Center for Tumor Diseases, University Hospital Heidelberg, German Cancer Research Center (DKFZ), Heidelberg, Germany

Correspondence to

Dr Sjoerd H van der Burg; shvdburg@lumc.nl

ABSTRACT

Background Primary and secondary resistance is a major hurdle in cancer immunotherapy. Therefore, a better understanding of the underlying mechanisms involved in immunotherapy resistance is of pivotal importance to improve therapy outcome.

Method Here, two mouse models with resistance against therapeutic vaccine-induced tumor regression were studied. Exploration of the tumor microenvironment by high dimensional flow cytometry in combination with therapeutic *in vivo* settings allowed for the identification of immunological factors driving immunotherapy resistance.

Results Comparison of the tumor immune infiltrate during early and late regression revealed a change from tumor-rejecting toward tumor-promoting macrophages. In concert, a rapid exhaustion of tumor-infiltrating T cells was observed. Perturbation studies identified a small but discernible CD163^{hi} macrophage population, with high expression of several tumor-promoting macrophage markers and a functional anti-inflammatory transcriptome profile, but not other macrophages, to be responsible. In-depth analyses revealed that they localize at the tumor invasive margins and are more resistant to Csf1r inhibition when compared with other macrophages. *In vivo* studies validated the activity of heme oxygenase-1 as an underlying mechanism of immunotherapy resistance. The transcriptomic profile of CD163^{hi} macrophages is highly similar to a human monocyte/macrophage population, indicating that they represent a target to improve immunotherapy efficacy.

Conclusions In this study, a small population of CD163^{hi} tissue-resident macrophages is identified to be responsible for primary and secondary resistance against T-cell-based immunotherapies. While these CD163^{hi} M2 macrophages are resistant to Csf1r-targeted therapies, in-depth characterization and identification of the underlying mechanisms driving immunotherapy resistance allows the specific targeting of this subset of macrophages, thereby creating new opportunities for therapeutic intervention with the aim to overcome immunotherapy resistance.

INTRODUCTION

Despite several major breakthroughs in the field of cancer immunotherapy, the road to

WHAT IS ALREADY KNOWN ON THIS TOPIC

⇒ Attempts to target tumor-associated macrophages with Csf1r-inhibiting therapies have met with disappointing clinical results. Recent studies show that specific small subsets of tissue resident M2-like macrophages are associated with poor clinical outcome.

WHAT THIS STUDY ADDS

⇒ We show that a small population of CD163^{hi} tissue-resident macrophages is responsible for primary and secondary resistance against T-cell-based immunotherapies as well as the underlying mechanisms. Notably, these CD163^{hi} M2 macrophages are resistant to Csf1r-targeted therapies.

HOW THIS STUDY MIGHT AFFECT RESEARCH, PRACTICE OR POLICY

⇒ Targeting of tumor-associated macrophages by Csf1r-inhibiting therapies does not affect those subsets of M2-like macrophages with a strong negative impact on T-cell-based immunotherapy outcomes. To reach clinical impact, new studies should focus on the exact identification of those macrophage subsets that impair tumor immunity and the development of therapeutic interventions specifically targeting these macrophage subsets.

ultimate success is obscured by therapy resistance. While some tumors are completely unresponsive to immunotherapy, others are initially successfully targeted as evidenced by substantial reduction in tumor burden, only to grow back at later stages.^{1,2} Understanding the underlying mechanisms involved in secondary immunotherapy resistance is therefore of pivotal importance to improve therapy outcome. Currently, knowledge on this is mostly limited to malfunctions of T cells (ie, checkpoint expression, T-cell exhaustion) or tumor-intrinsic mechanisms, including problems in the tumor antigen

presentation pathway, mutations in immune signaling pathways and resistance to killing.³ In addition, there is much speculation on the effects of tumor-extrinsic resistance mechanisms, including the action of immunosuppressive inflammatory cells at the tumor site, because of their association with bad prognosis^{3–5} but clear evidence still is lacking. Major problems in studies on secondary resistance mechanisms are the limitation in human pretreatment and post-treatment samples, anecdotally revealing an escape mechanism^{6,7} and the use of mouse tumor models most often showing immunotherapy-mediated delayed tumor outgrowth rather than tumor regression, thus failing to replicate the clinical observations and the potential to discover how secondary resistance is mediated.^{8–10} We hypothesized that this limitation could be tackled by using two preclinical tumor models in which primary tumor regression is induced by stimulation of tumor-specific T-cell activity using therapeutic vaccination, followed by immune escape, in combination with detailed studies of the tumor microenvironment (TME) during different stages of their response to immunotherapy.

RESULTS

A more effective therapeutic response is associated with the intratumoral presence of functionally different CD8⁺ T cells and macrophages

Two therapeutic vaccination strategies to treat established TC-1 tumors with the Human Papillomavirus (HPV)16 E7_{43–63} synthetic long peptide (SLP) and CpG have been developed.¹¹ In strategy 1, mice are vaccinated with the SLP, CpG and Incomplete Freund's Adjuvants in the contralateral flank. In the second strategy, mice are vaccinated with the SLP and CpG administered in the tail base, causing the vaccine to reach the tumor draining lymph nodes in both flanks (figure 1A). Vaccination according to strategy 1 allows the tumors to become larger before tumor regression sets in and does not lead to (near) complete regressions as observed after vaccination strategy 2 (figure 1B). Comparison of the TME at the time of therapeutic response (day 16) in both vaccination settings revealed profound differences. The TME after vaccination strategy 2 was characterized by a lower infiltration of immune cells, including pDC, cDC1, B cells, NK cells and T cells into the tumor (figure 1C, online supplemental figure S1A,B). Additionally, the CD8⁺ T cells have a more naïve and less effector memory phenotype, as determined by CD62L and CD44 expression. Further characterization of the T_n, T_{cm} and T_{em} phenotype following vaccination strategy 2 revealed enrichment in non-classical naïve CD8⁺ T cells,¹² characterized by high expression of CD27 and intermediate expression of CD122 and Eomes (online supplemental figure 1C). Furthermore, the CD8⁺ T cell population comprises less cells expressing co-inhibitory markers, CD49a, and CD122, while co-stimulation (CD28) and their proliferative capacity (Ki-67) was increased (figure 1D, online

supplemental figure S2). Although the percentage of macrophages is not significantly different, their phenotype is affected by the different vaccination strategies as demonstrated by a lower percentage of SIRP α ⁺ and CD11c⁺ macrophages and higher numbers of iNOS⁺ and Ly6C⁺ macrophages after vaccination strategy 2 (figure 1E, online supplemental figure S2). This not only suggests that a less effective antitumor response (strategy 1) requires a stronger recruitment and activation of many members of the immune system to enable a therapeutic response, but also implies that a lower yet more functional T cell and macrophage response (strategy 2) is more effective in controlling tumor growth.

Antitumor function of intratumoral CD8⁺ T cells and macrophages is rapidly lost during tumor regression

To gain a better insight in the development of the exhausted immune response after vaccination strategy 1, the changes in the TME were studied over time following therapeutic response to vaccination. Tumors were isolated and analyzed by high dimensional flow cytometry directly after the response to therapy set in, and 3 days later (figure 2A). Remarkably, the composition of the TME was completely altered within these 3 days. Analysis of both the myeloid and lymphocytic cell compartments revealed a lack of co-clustering when the two different days were compared, indicating dramatic changes in the cellular characteristics (figure 2B, online supplemental figure S2). Detailed analysis revealed a strong reduction in the percentage of macrophages (figure 2C, online supplemental figure S2). Additionally, these macrophages switched to an immunosuppressive phenotype based on the increased expression of Arginase 1 (Arg1) and SIRP α and the loss of iNOS, MHC-II and CD40 (figure 2D, online supplemental figure S2). Profound changes in the CD8⁺ T-cell population were observed, indicative for an increased but less functional T-cell response (figure 2E, online supplemental figure S2). Three days after the start of tumor regression, more of the CD8⁺ T cells express the co-inhibitory markers CD39, NKG2A, CTLA-4 and TIGIT while the expression of the inflammatory molecule CD49a is decreased. Furthermore, the CD8⁺ T_{cm} population evaporated, suggestive of excessive drainage on these precursors for effector cells and fitting with their increased expression of the proliferation marker Ki-67. Loss of the transcription factor Eomes indicates a potential decrease in type 1 T cells. Thus, the less effective tumor control and eradication induced by vaccine strategy 1 is associated with a rapid loss of antitumor immune function, due to exhaustion of intratumoral T cells and loss of immunostimulatory capacity of macrophages.

CD163^{hi} macrophages bear a distinct anti-inflammatory phenotype and are resistant to Csf1-targeted therapy

The increased expression of several co-inhibitory molecules may call for the use of immune checkpoint inhibitors to improve therapeutic efficacy, but we showed previously that checkpoint inhibition displayed only marginal effects

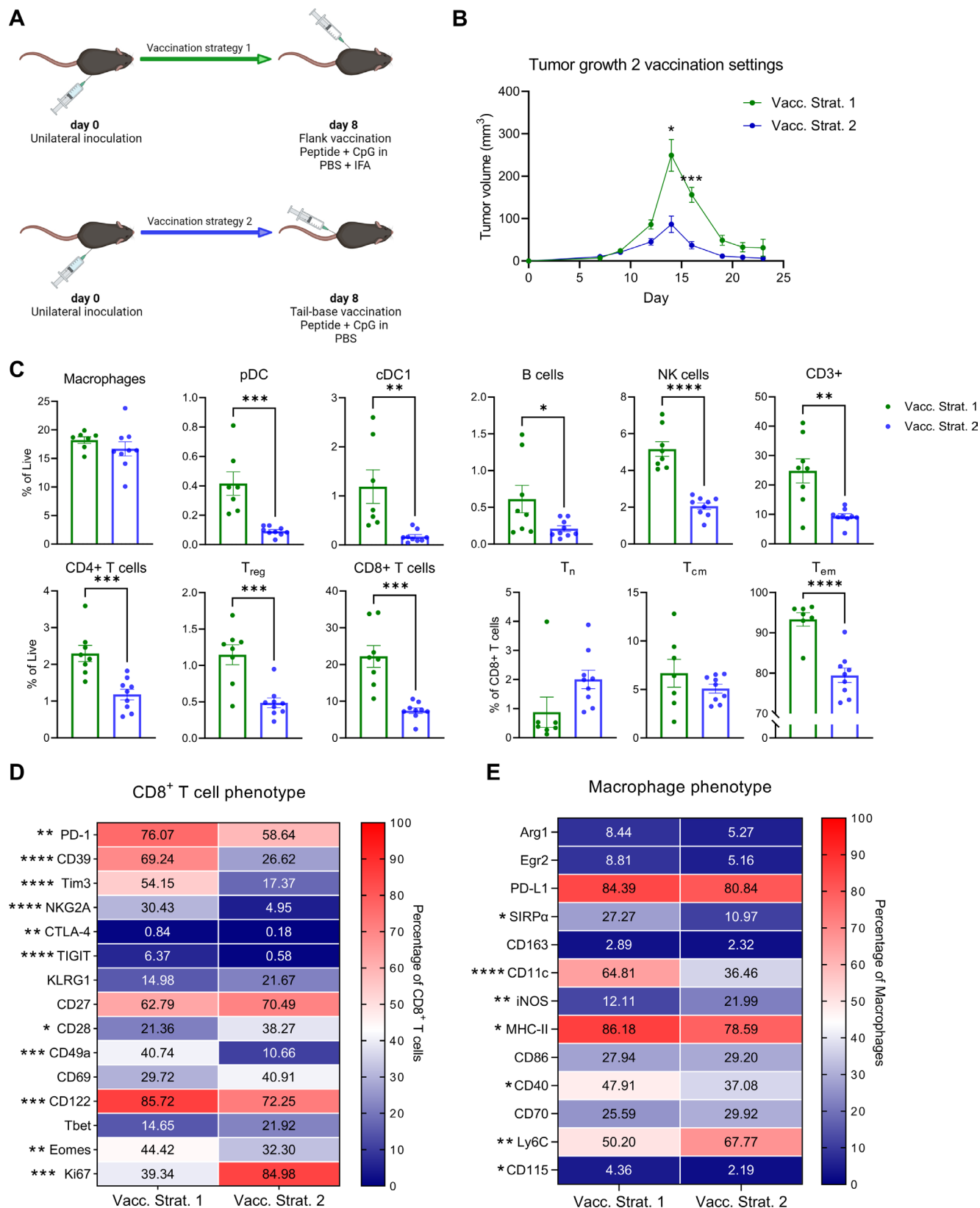


Figure 1 A lower yet more functional T cell and macrophage response is associated with enhanced tumor control. (A) Experimental setup of therapeutic vaccination strategies for TC-1 tumors. (B) Average tumor growth curves of TC-1 tumors treated with vaccination strategy 1 or 2 (n=10 per group). (C) Percentages of myeloid and lymphoid populations in the TME and percentages of naïve, central memory and effector memory CD8⁺ T cells, 8 days after therapeutic vaccination (n=7–9 per group). (D, E) Heatmap representing the percentages of CD8⁺ T cells and macrophages expressing phenotypic markers in the TME 8 days after therapeutic vaccination (n=7–9 per group). IFA, Incomplete Freund's Adjuvants; PBS, Phosphate Buffered Saline; TME, tumor microenvironment. Significance is shown as * $p < 0.05$, ** $p < 0.01$, *** $p < 0.001$ and **** $p < 0.0001$.

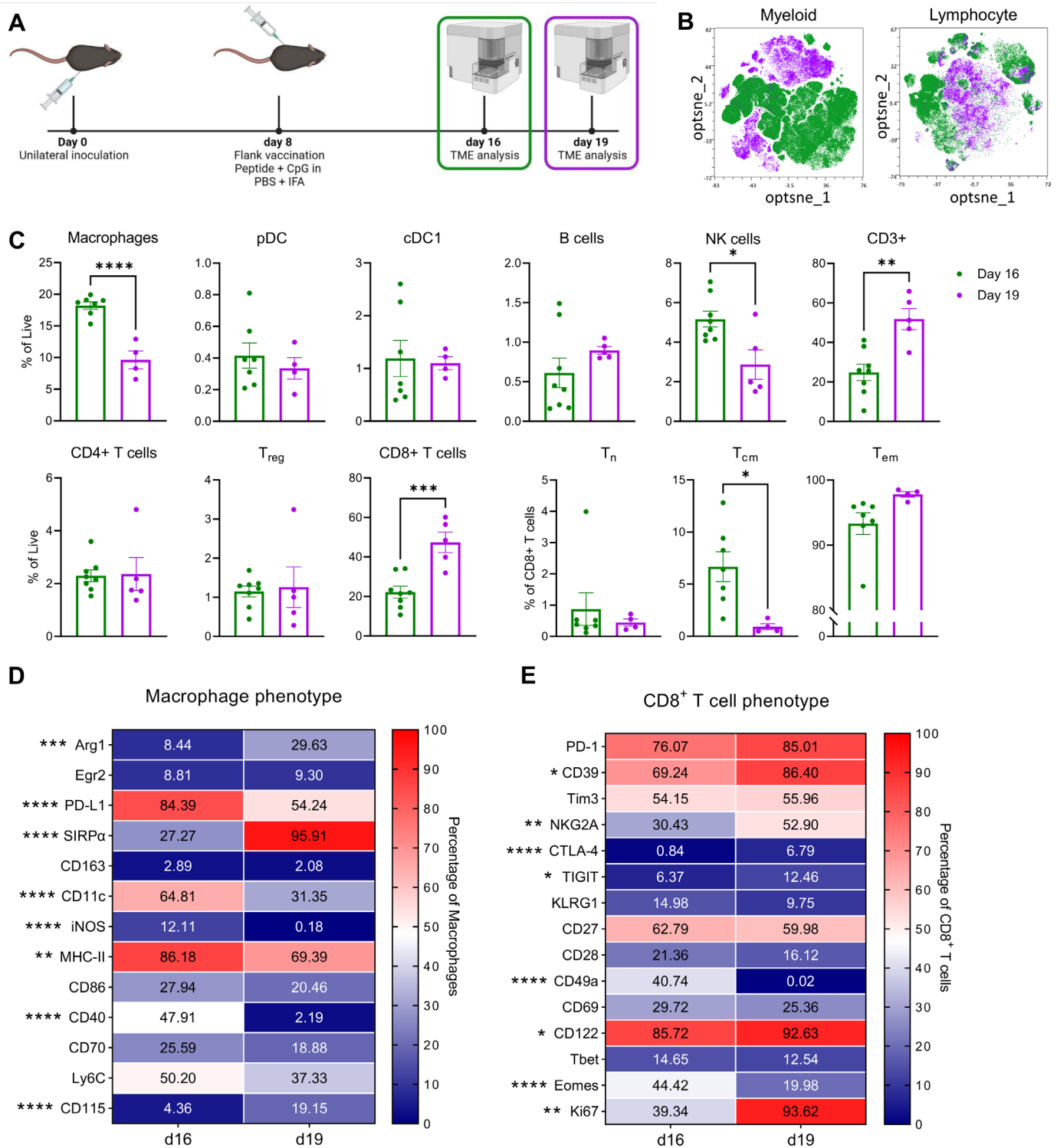


Figure 2 Ineffective tumor control and eradication is associated with a rapid loss of immune function. (A) Experimental setup of a TME study comparing therapeutically vaccinated mice at day 16 and 19 after tumor inoculation. (B) opt-SNE plots of myeloid and lymphocyte compartments from day 16 (green) and 19 (purple) (C) Percentages of myeloid and lymphocyte populations as well as naïve, central memory and effector memory CD8⁺ T cells in the TME at day 16 (green) and 19 (purple). (D, E) Heatmap representing the percentages of macrophages and CD8⁺ T cells expressing phenotypic markers in the TME at day 16 and 19 after tumor inoculation (n=5–8 per group). TME, tumor microenvironment; t-SNE, t-Distributed Stochastic Neighbor Embedding. Significance is shown as *= $p < 0.05$, **= $p < 0.01$, ***= $p < 0.001$ and ****= $p < 0.0001$.

on tumor control in this model.^{11 13} Tumor-associated macrophages (TAMs) have also been widely described to promote tumor progression. The rapid switch from an

immune stimulatory to immunosuppressive macrophage phenotype prompted us to interrogate their role in the loss of intratumoral immune function. First, the key

regulator of myeloid differentiation and function Csf1 was targeted using PLX-3397, a selective Csf1r (CD115) and c-Kit inhibitor. However, this impaired the response to therapeutic vaccination and no vaccine-driven tumor regressions could be observed (online supplemental figure S3A,B), validating the importance of the functional switch observed in macrophages with respect to tumor control (figures 1E and 2D). Treatment with PLX-3397 also resulted in a significant reduction in pDC, cDC1, B, NK and T cells, but not T_{reg} cells (online supplemental figure S3C-E). To target the potential immune suppressive macrophages more specifically, they were characterized using established immunosuppressive M2-like phenotypic markers, including CD163, Arg1, Egr2, PD-L1, SIRP α and SiglecG. Two CD163⁺ macrophage populations could be distinguished, one with intermediate levels of CD163 (CD163^{dim}) and one with high levels of CD163 (CD163^{hi}; figure 3A). Phenotypically, the CD163⁺, CD163^{dim} and CD163^{hi} macrophages were very distinct, with the CD163^{hi} population bearing the classical immunosuppressive M2 phenotype Arg1⁺Egr2⁺PD-L1⁺SIRP α ⁺SiglecG⁺ (figure 3B). Analysis of the spatial organization of the macrophages in these tumors by immunohistochemistry revealed an almost complete reduction in macrophages (F4/80) by PLX-3397, except for a fraction at the invasive tumor margin (figure 3C,D, online supplemental figure S4A) where most of the CD163^{hi} macrophages resided, as tissue-resident macrophages surrounding the tumor. Besides the CD163^{hi} macrophages in the tumor margin, some CD163⁺ cells were present inside the tumor. These cells stained weaker against CD163 and are assumed to be the CD163^{dim} macrophages, in accordance with Etzerodt *et al.*¹⁴ Together, this indicated that tissue-resident CD163^{hi} macrophages are more resistant to Csf1-targeted therapy than other macrophages and implied the requirement for a more direct approach to deplete them.

CD163^{hi} macrophages drive both primary and secondary immunotherapy resistance

The use of doxorubicin-loaded CD163-directed liposomes (α CD163-DXR) allows the specific depletion of CD163⁺ macrophages in tumors, while empty liposomes (α CD163-Control) leave this population intact.^{14 15} This was confirmed by immunohistochemistry (figure 3C,D, online supplemental figure S4A). No direct effects of the CD163-directed liposomes on the number or phenotype of tumor cells were found *in vivo* (online supplemental figure S4B). On-target off-tumor toxicity of α CD163-DXR was assessed in heart, kidney and liver tissue (online supplemental figure S5). As expected, CD163⁺ macrophages can be found in heart and liver tissue, but are absent from the kidneys. Treatment with α CD163-DXR did not target cardiac CD163⁺ macrophages, but did result in a decrease in CD163⁺ cells in the liver. Nevertheless, this decrease did not impact total macrophage numbers in the liver, and as no evident pathologies arose during experiments, the safety of this treatment was deemed acceptable. Strikingly, when α CD163-DXR was combined

with vaccine strategy 1 the depletion of CD163⁺ macrophages recapitulated the differences in tumor control between the two vaccine strategies as it led to better control of tumor growth by vaccine strategy 1, similar to previously observed with vaccine strategy 2 (figure 4A,B). Therefore, we used this approach to study the impact of CD163⁺ macrophages on the changes observed in the TME and survival of mice.

Exploration of the TME by high dimensional flow cytometry following CD163⁺ macrophage depletion in TC-1 tumors revealed subtle changes in the t-Distributed Stochastic Neighbor Embedding (t-SNE) clustering of myeloid and pronounced changes in the lymphocyte populations (figure 4C, online supplemental figure S6). A specific depletion of CD163^{dim} and CD163^{hi} macrophages was confirmed by flow cytometry, while the total percentage of macrophages remained intact (figure 4D,E), as would be expected since the CD163⁺ macrophage population only forms a small fraction within the total population of macrophages. CD163⁺ macrophage depletion did not alter the number of tumor-infiltrating T cells (figure 4E) but had a major effect on the phenotype of tumor-infiltrating CD8⁺ T cells (figure 4F,G, online supplemental figure S6), highly resembling to the TME of tumors treated with the more effective vaccination strategy 2 (figure 1). Specifically, the number of effector cells, and percentage of HPV-specific tetramer-positive cells decreased. Notably, the T_{eff}^+/T_{reg} and Tm^+/T_{reg} ratios remained unaltered. The number of effector CD8⁺ T cells decreased while the non-classical naïve CD8⁺ T cells increased, an immune cell composition in the TME that is highly similar to the one found with vaccination strategy 2 (figure 1, online supplemental figure S1C,S7). Also the expression of all co-inhibitory molecules, CD28, CD122 and CD49a on total CD8⁺ T cells was decreased. The impact on the remaining macrophages was subtle with a significant decrease in PD-L1⁺ cells and increase in the expression levels of the M1-like marker iNOS (figure 4H).

Where checkpoint targeted therapies failed to prevent tumor recurrence (online supplemental figure 8A) and despite the fact that CD163⁺ macrophages only make up a small percentage of total macrophages, depletion of these cells resulted in a significant clinical improvement when mice were also vaccinated. This was evidenced by a strongly decreased tumor relapse rate, as only 4/17 mice relapse in the CD163 depletion group, compared with 12/17 mice in the control group (figure 5A,B). Consequently, the overall survival was greatly improved, with the survival rate going up from ~29% to ~76% (figure 5C,D). Depletion of CD163⁺ macrophages as a single treatment had no effect (figure 5B-D).

To confirm the key role of CD163⁺ macrophages in extrinsic immunotherapy resistance, their involvement in the Rauscher's Murine Leukemia virus induced RMA-Qa-1^{-/-} tumor model, genetically modified to block the immune checkpoint axis NKG2A/Qa1, was tested.¹³ Therapeutic vaccination with the Gag-encoded CD8⁺ T-cell

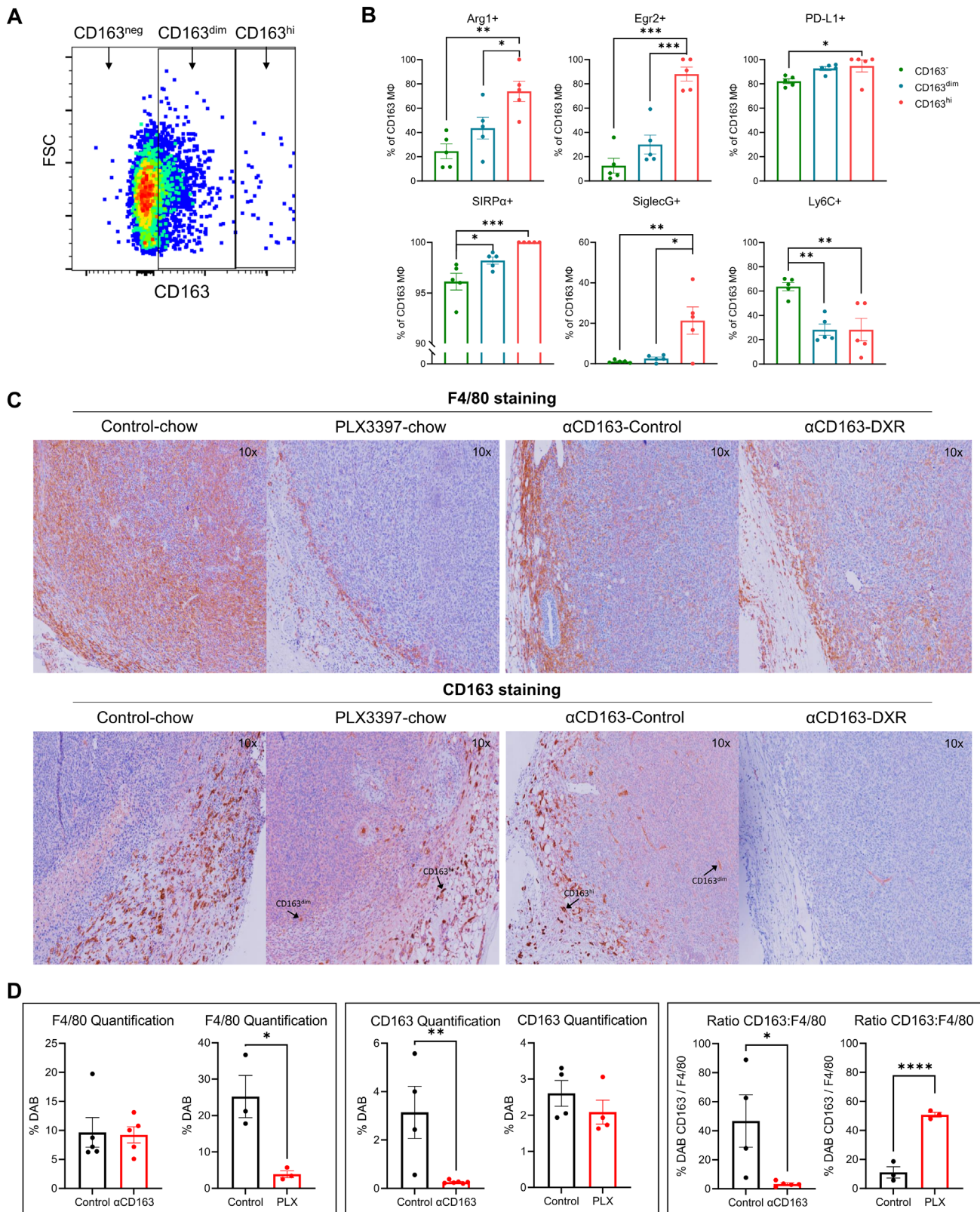


Figure 3 CD163^{hi} macrophages bear a classical anti-inflammatory M2-like phenotype and are resistant to Csf1-targeted therapy. (A) Representative flow cytometry dot plot of CD163 expression on macrophages in the TME. (B) Expression of macrophage-associated markers on CD163^{neg}, CD163^{dim} and CD163^{hi} macrophages (n=5 per group). (C) Representative immunohistochemistry staining of macrophages (F4/80, top) and CD163⁺ cells (bottom) in tumors treated with αCD163-DXR or PLX3397 and their respective controls, 10x zoom. (D) Immunohistochemistry DAB quantification of F4/80 (left panel), CD163 (middle panel) or CD163/F4/80 ratios (right panel) of tumors after treatment with αCD163-DXR or PLX3397 (n=3–5 per group). DAB, 3,3'-diaminobenzidine; TME, tumor microenvironment. Significance is shown as **p*<0.05, ***p*<0.01, ****p*<0.001 and *****p*<0.0001.

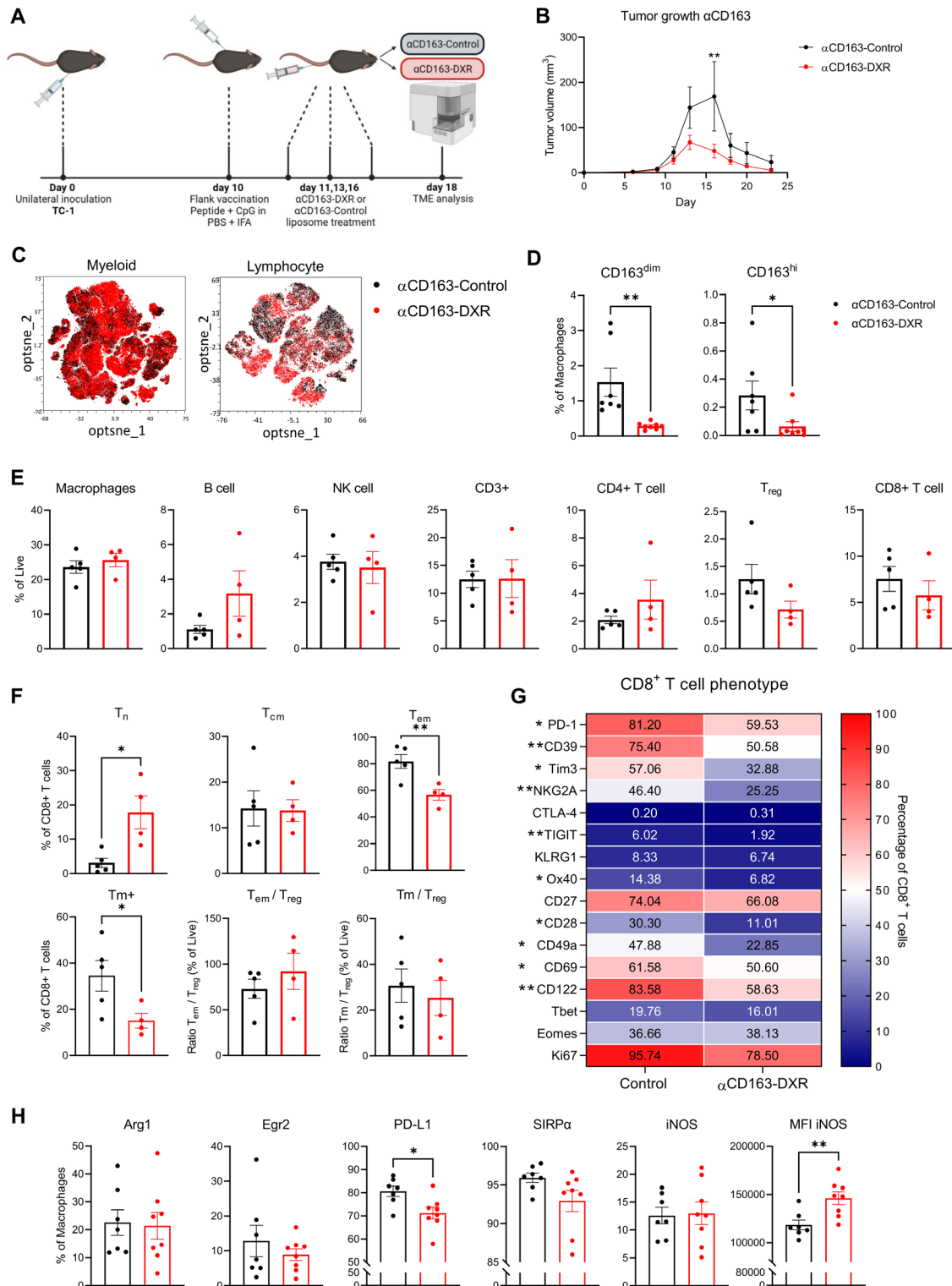


Figure 4 CD163⁺ macrophage depletion reverses the hyperactivated phenotype of CD8⁺ T cells. (A) Experimental setup of a TME study comparing therapeutically vaccinated mice treated with α CD163-Control liposomes (black) to mice treated with α CD163-DXR depleting liposomes (red) (B) Average tumor growth curves of TC-1 tumors treated with therapeutic vaccination in combination with α CD163-Control liposomes (black) or α CD163-DXR depleting liposomes (red; n=17 per group) (C) opt-SNE plots of myeloid and lymphocyte compartments of tumors treated with therapeutic vaccination in combination with α CD163-DXR or control nanoparticles. (D–F) Percentages CD163^{dim} and CD163^{hi} macrophages of total macrophages (D) myeloid and lymphocyte populations (E) and effector state of CD8⁺ T cells (F) from tumors with (red) and without (black) CD163⁺ macrophage depletion (n=4–5 per group). (G) Heatmap representing the percentages of CD8⁺ T cells expressing phenotypic markers in the TME of control and α CD163-DXR treated tumors (n=4–5 per group). (H) Percentage and Mean Fluorescent Intensity (MFI) of macrophages expressing M2-like (Arg1, Egr2, PD-L1, SIRP α) and M1-like (iNOS) phenotypic markers in the TME (n=4–5 per group). MFI, Mean Fluorescent Intensity; TME, tumor microenvironment. Significance is shown as * p <0.05 and ** p <0.01.

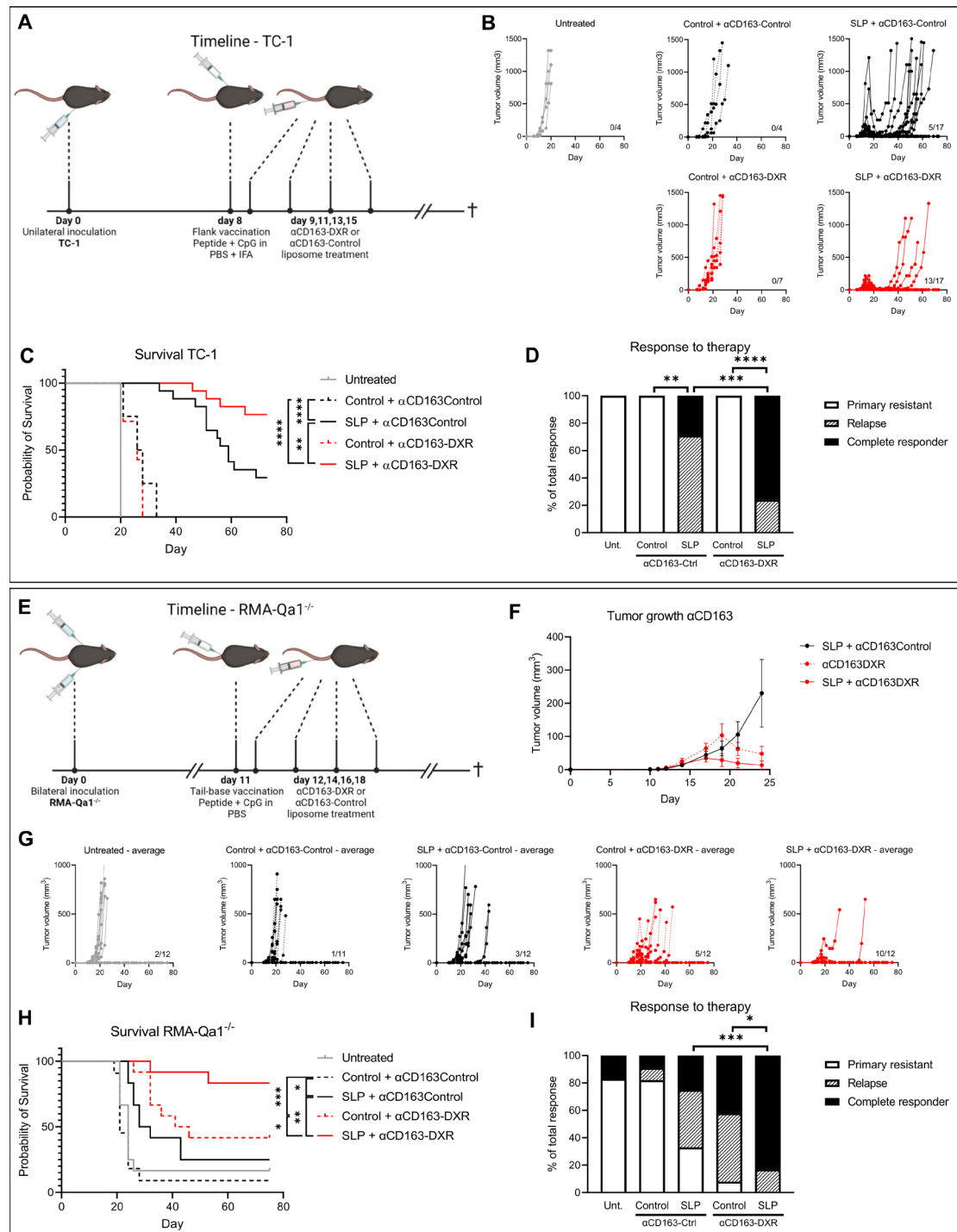


Figure 5 CD163⁺ macrophage depletion overcomes primary and secondary resistance against immunotherapy. (A) Experimental timeline of TC-1 tumor-bearing mice treated with therapeutic vaccination in combination with α CD163-Control or α CD163-DXR liposomes. (B) Tumor growth curves of TC-1 tumors from untreated (gray), α CD163-Control liposome single treated (black dashed), therapeutic vaccination with α CD163-Control liposomes (black), α CD163-DXR liposome single treated (red dashed) or therapeutic vaccination and α CD163-DXR liposome (red) treated mice (n=4–17 per group). Numbers represent the animals that are tumor free at the end of the study. (C) Survival curve and (D) response bar graphs of TC-1 tumor-bearing mice treated with therapeutic vaccination and α CD163-DXR liposomes or their respective controls (n=4–17 per group). (E) Experimental timeline of RMA-Qa1^{-/-} tumor-bearing mice treated with therapeutic vaccination in combination with α CD163-Control or α CD163-DXR liposomes. (F) Average tumor growth curves of RMA-Qa1^{-/-} tumors treated with therapeutic vaccination in combination with α CD163-Control liposomes (black) or α CD163-DXR depleting liposomes (red) or α CD163-DXR depleting liposomes single treatment (red dashed) (n=11–12 per group). (G) Tumor growth curves of RMA-Qa1^{-/-} tumors treated with therapeutic vaccination and α CD163-DXR liposomes or their respective controls (H) Survival curve and (I) response bar graphs of RMA-Qa1^{-/-} tumor-bearing mice treated with therapeutic vaccination and α CD163-DXR liposomes or their respective controls (n=11–12 per group). Significance is shown as * p <0.05, ** p <0.01, *** p <0.001 and **** p <0.0001.

epitope and the Env-encoded CD4 T-cell epitope may result in strong but transient therapeutic responses in a bilateral tumor growth setting as used here. Some tumors are primary resistant against therapy, while others initially regress before they relapse. Therefore, this model is ideal to study primary and secondary resistance against immunotherapy. Similar to the TC-1 tumor model, depletion of CD163⁺ macrophages in RMA-Qa1^{-/-} strongly improved immunotherapy induced tumor control (figure 5E,F). Unlike the results obtained in the TC-1 tumor model, depletion of CD163⁺ macrophages in RMA-Qa1^{-/-} as single therapy already results in strong tumor regressions (figure 5F). This is accompanied by a significant increase in T cells and NK cells in the TME (online supplemental figure S8B-D). More specifically, the type 1 phenotype of CD8⁺ T cells is enriched, marked by increased Eomes and GrzB expression as well as proinflammatory cytokine production (online supplemental figure S8E). The individual tumor growth curves from RMA-Qa1^{-/-} reveal that CD163⁺ macrophage depletion not only impacts primary tumor outgrowth, but also overcomes secondary immunotherapy resistance after therapeutic vaccination, with tumor relapse in only 2/12 mice in the CD163 targeted group vs 9/12 in the control group (figure 5G). Accordingly, the survival rate increases from 25% to 83% when mice were treated with the combination of CD163⁺ macrophage depletion and therapeutic vaccination as compared with vaccination alone (figure 5H,I). Together, these findings demonstrate that the tumor-resident CD163⁺ macrophages are key in mediating primary and secondary resistance to immunotherapy.

The wound healing features of CD163^{hi} macrophages are involved in immune suppression and therapy resistance

To dissect the cellular processes in the immunotherapy resistance-causing CD163⁺ macrophages, we isolated CD163⁺, CD163^{dim} and CD163^{hi} macrophages from TC-1 tumors and compared their transcriptomic phenotype by bulk RNA sequencing. Principal component analysis revealed a distinct clustering of these three cell types, with the CD163^{dim} cells appearing to be of an intermediate phenotype, bearing some similarity to both CD163⁺ and CD163^{hi} macrophages (figure 6A). The expression of genes associated with true M2 macrophage function, including *Fcbr2*, *Mmp12*, *Arg1*, *Ccl8*, *Cd15*, *Ido1*, *Il10*, *Cebpa*, *Retnla*, *Pparg*, *Nfe2l2*, *Itgax*, *Hmox1*, *Mrc1* and *Maf*, was strongly increased in CD163^{hi} macrophages when compared with CD163^{dim} and even stronger when compared with CD163⁺ macrophages (figure 6B, online supplemental data files 1,2), indicating that the CD163^{hi} macrophages are functionally polarized immunosuppressive M2 macrophages.^{16,17} While the CD163^{dim} macrophages express some characteristic M2-polarized macrophage genes (eg, *Irf4*, *Cebpd*, *Il33*), these cells clearly are not functional immunosuppressive M2 macrophages as can be deduced from their expression of gene transcripts for IFN γ and granzymes. This fits well with reports

indicating that not all CD163⁺ cells are truly M2-polarized macrophages and may even be dendritic cells.^{18,19}

Since the CD163⁺ macrophage population consists of all other macrophages present in the TME and is therefore very heterogeneous, we focused on the DEGs between CD163^{hi} and CD163^{dim} macrophages. We performed a gene set enrichment analysis (GSEA)-based enrichment for GO-terms on these DEGs and subsequently ran these GO terms (251 total) with their respective p-adjusted values through the REVIGO software to remove redundant GO terms.²⁰ The results were then plotted in Cytoscape (figure 6C) and revealed three main pathways enriched in CD163^{hi} macrophages compared with CD163^{dim} macrophages: (1) blood vessel development, (2) extracellular matrix (ECM) remodeling, and (3) wound healing (online supplemental data file 3). Macrophages, especially of tissue-resident origin, have been described to play a role in blood vessel development.²¹ We therefore studied the presence of intratumoral blood vessels by immunohistochemistry staining against CD31.²² However, depletion of CD163⁺ macrophages did not alter the number of blood vessels, as quantified by CD31 DAB (3,3'-diaminobenzidine) staining (figure 7A, online supplemental figure S9A) indicating that this pathway did not play a role in therapy resistance. This notion was confirmed by depletion of all CD115⁺ macrophages using PLX3397, where a significant reduction in the number of intratumoral blood vessels was observed. To investigate the effect on ECM remodeling, tumors from mice treated with α CD163-Control or α CD163-DXR were stained using the Masson's Trichrome Stain Kit. Indeed, a decrease in the collagen deposit could be observed on depletion of CD163⁺ macrophages (figure 7B, online supplemental figure S9B). However, TC-1 tumors in general are very low in collagen, as compared with KPC3 tumors or skin tissue, making it highly unlikely that the impact of ECM remodeling sensitized TC-1 tumors to immunotherapy. One of the mechanisms by which macrophages can execute their wound healing capacity acts via heme oxygenase 1 (HO-1), with as result the release of the anti-inflammatory metabolites iron, carbon oxide and biliverdin, which leads to the production of the well-known immunosuppressive compound adenosine and the upregulation of CD39 on T cells.^{23,24} Examination of the genes associated with the wound healing pathway showed that *Hmox1*, the gene encoding for HO-1 and its transcription factor Nfe2l2 (*Nrf2*) were specifically upregulated in the CD163^{hi} macrophage population (figure 6B). Indeed, depletion of CD163⁺ macrophages by α CD163-DXR resulted in a significant decrease in HO-1 when compared with control treatment, as determined by immunohistochemistry staining (figure 7C,D). Therefore, Tin Protoporphyrin IX dichloride (SnPP), a specific HO-1 inhibitor, was used in combination with therapeutic vaccination to treat TC-1 tumor-bearing mice. Similar to treatment with the more effective vaccination strategy 2 or depletion of CD163⁺ macrophages, inhibition of HO-1 improved the initial tumor control by vaccination strategy

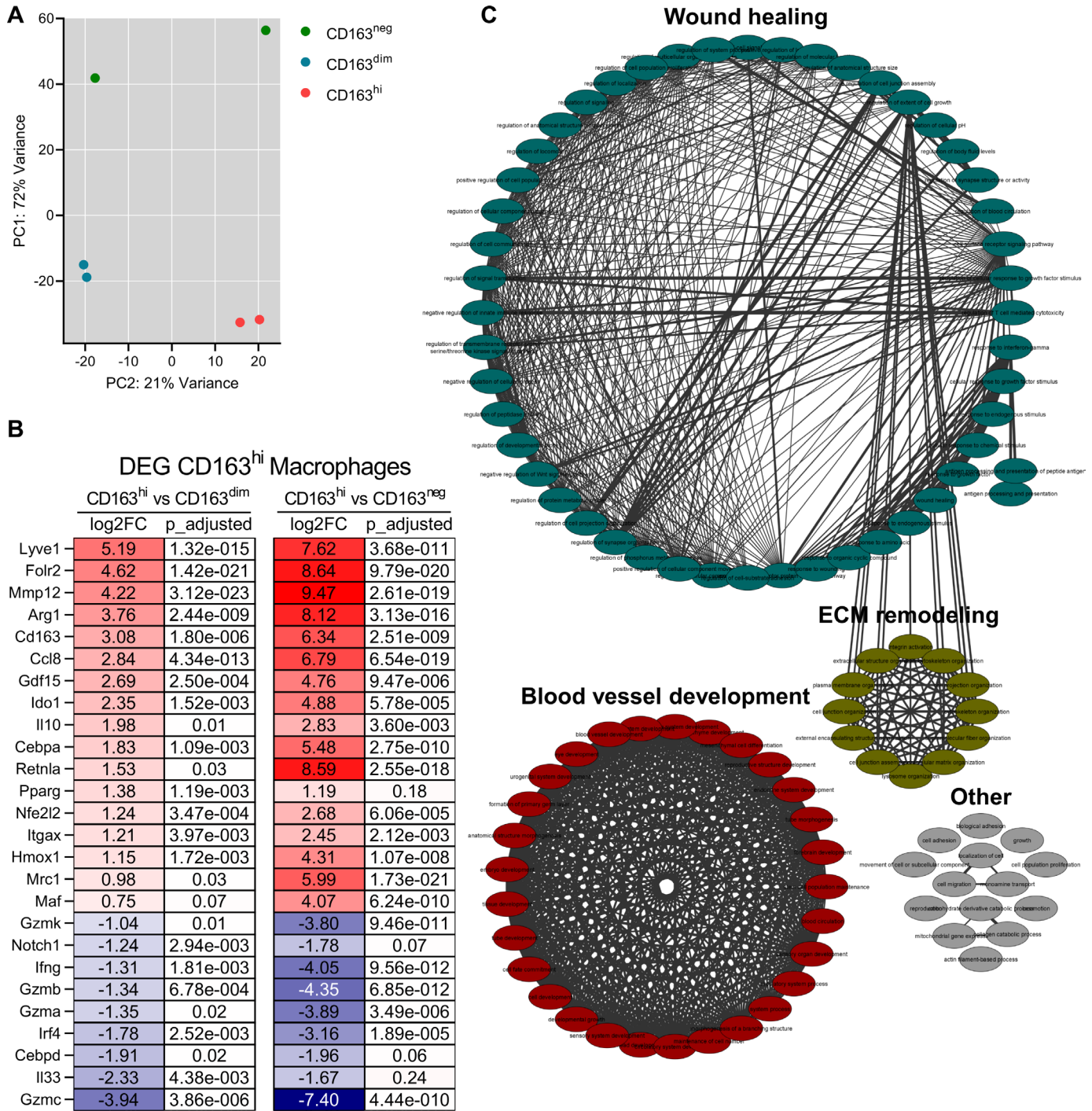


Figure 6 CD163^{hi} macrophages are involved in wound healing, blood vessel development and ECM remodeling. (A) PCA plot of sorted CD163^{hi}, CD163^{dim} and CD163⁻ macrophages from the TME of TC-1 tumors treated with therapeutic vaccination, as determined by bulk RNA sequencing. (B) Heatmap of highlighted differentially expressed genes (DEG) with the log₂ Fold Change (log₂(CD163^{hi})-log₂(CD163^{dim})) (left) and the log₂ Fold Change (log₂(CD163^{hi})-log₂(CD163⁻)) and their adjusted p values. (C) REVIGO analysis of enriched GO terms in CD163^{hi} macrophages compared with CD163^{dim} macrophages, figure created in Cytoscape using a circular layout. ECM, extracellular matrix; PCA, principal component analysis.

1, resulting in (near) complete regressions (figure 7E). Additionally, a strong decrease in the number of tumor relapses could be observed (figure 7F,G) and the survival rate of mice was significantly improved in comparison to SnPP or vaccination single treatment (figure 7H).

Similar to tumors treated CD163⁺ macrophage depletion, treatment with SnPP did not increase the number

of tumor infiltrating CD8⁺ T cells but rather resulted in a phenotypic switch (online supplemental figure 10A-D). This included the increase in infiltration by non-classical naïve CD8⁺ T cells and a decrease in the expression of co-inhibitory molecules, CD28 and CD49a. The phenotype of the macrophages was not altered by HO-1 inhibition (online supplemental figure 10E). The observed

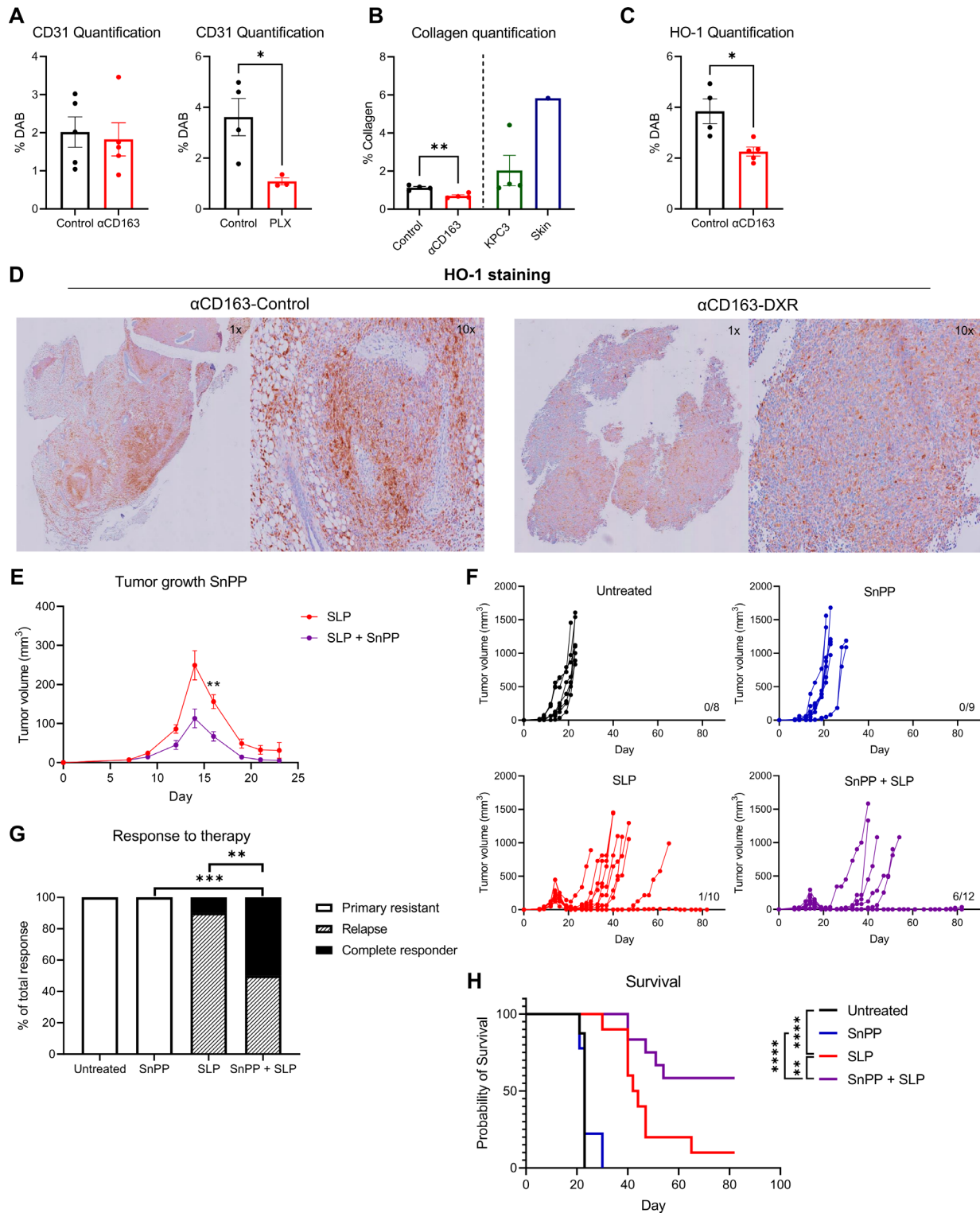


Figure 7 CD163^{hi} macrophages drive immunotherapy resistance via HO-1. Immunohistochemistry DAB quantification in TC-1 tumors treated with therapeutic vaccination in combination with α CD163-Control or α CD163-DXR liposomes (left) or in combination with control or PLX3397 (right) for (A) CD31, (B) collagen and (C) HO-1 (n=4–5 per group). (B) Collagen staining of KPC3 tumors (green) and mouse skin (blue) are positive controls (n=1–5). (D) Representative immunohistochemistry staining of HO-1 in tumors treated with α CD163-Control (left) or α CD163-DXR (right), 1x and 10x zoom. (E) Average tumor growth curves of TC-1 tumors treated with therapeutic vaccination (red) or therapeutic vaccination and SnPP (purple) (n=10–12 per group). (F) Tumor growth curves of TC-1 tumors from untreated (black), SnPP treated (blue), therapeutic vaccination treated (red) or SnPP and therapeutic vaccination (purple) treated mice (n=8–12 per group). Numbers represent the animals that are tumor free at the end of the study. (G) Bar graph representing response to therapy and (H) survival graph of TC-1 tumor-bearing mice treated with therapeutic vaccination and SnPP or their respective controls (n=8–12 per group). SLP, synthetic long peptide. Significance is shown as *= p <0.05, **= p <0.01 and ***= p <0.001.

effects of the HO-1 inhibitor on CD8⁺ T cells appear to be indirect, as the expression of the co-inhibitory molecules changed *in vivo*, were not altered when CD8⁺ T cells in CD3/CD28 activated splenocytes cultured in the presence of the HO-1 inhibitor SnPP were compared with those cultured without the HO-1 inhibitor (online supplemental figure 10F). Together, these findings indicate that the wound healing pathway via increased HO-1 expression, is one of the mechanisms employed by the tissue-resident CD163⁺ functional M2 macrophages to drive immunotherapy resistance.

CD163^{hi} macrophages resemble a specific monocyte/macrophage population in humans

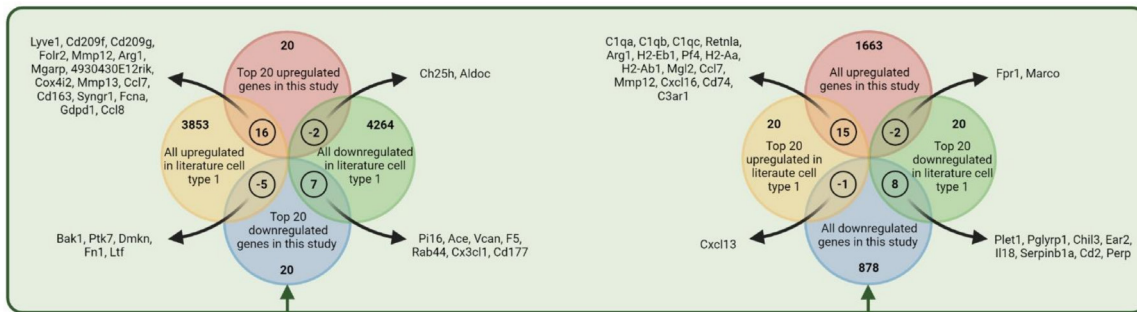
Recently, a number of transcriptomic profiles of different types of macrophage and myeloid cells have been reported, which allowed us to compare the transcriptomic profile of the CD163^{hi} macrophage population with these populations. The expression of the top 20 upregulated and downregulated genes from the CD163^{hi} macrophage dataset was examined in the 14 established monocyte and macrophage types from literature (figure 8, left column). We devised a scoring system in which the presence and direction of an expressed gene within the top 20 of upregulated/downregulated genes in the CD163^{hi} and comparator population led to a maximum score of 80 points when the cell types displayed a highly similar transcriptomic profile (figure 8, right columns). From all of these types one monocyte/macrophage population, existing both in mice and humans, was highly similar to our CD163^{hi} macrophages. While the exact function of that similar monocyte/macrophage population has not been fully explored, they both display a functional M2 signature, suggesting the translational potential for targeting CD163^{hi} macrophages as a therapeutic intervention to overcome immunotherapy resistance in patients with cancer. As expected, inflammatory monocytes had the lowest similarity score to the CD163^{hi} macrophages from this study, confirming the anti-inflammatory M2-like nature of these macrophages. Interestingly, also cardiac macrophages were of fairly high similarity to the CD163^{hi} macrophages from this study, while splenic macrophages were of very low similarity. This underpins the tissue-resident nature of the CD163^{hi} macrophage population and explains their localization at the tumor invasive margin (figure 3C, online supplemental figure S4A). The previously with metastasis associated tumor-resident CD163⁺Tim4⁺ macrophages²⁵ did not match the CD163^{hi} macrophage population, fitting with the differences in Csf1r-targeted therapy sensitivity between the two cell types and underlines the heterogeneity of CD163⁺ macrophage populations as well as the necessity of additional phenotypic identifiers on top of CD163. To confirm the presence of a CD163^{hi} macrophage population in humans, we compared our CD163^{hi} gene set to established monocyte and macrophage populations from human datasets using the cellxgene MoMac_VERSE software. Indeed, a similar population was enriched in human cancers especially

in breast and pancreatic cancers (online supplemental figure S11A,B), which are notorious for their resistance to immunotherapy. These cells were most similar to anti-inflammatory macrophages, in particular to HES1⁺ TAMs (online supplemental figure S11C).²⁶ Altogether, these data confirm the presence of macrophage populations that are similar to the CD163^{hi} macrophages in human beings, and suggest that they play a similar role in human cancers.

DISCUSSION

Despite the initial impact of immunotherapy on tumor growth, patients often progress due to the development of therapy resistance. Here, we identified a small subset of CD163⁺ tissue-resident macrophages that drives both primary and secondary resistance against T cell-targeted immunotherapies in preclinical models. These macrophages were highly comparable to a subset of human macrophages with a functional M2 macrophage signature,²⁷ that is, enriched in human cancers and shares the expression of *Maf* in the CD163⁺ macrophage subset recently associated with low response to checkpoint therapy in patients with leukemia²⁸ as well as the lack of *Csf1r* expression in the CD163⁺ macrophage subset associated with resistance to checkpoint therapy in patients with non-small cell lung cancer.²⁹ While TAM heterogeneity in function and origin is widely acknowledged, macrophages are often grouped on the basis of a few markers.³⁰ Yet, recent studies show that among all macrophages present in tumors, small but different subsets of tissue-resident M2-like macrophages bear a strong impact on clinical progression^{25 27 31 32} and immunotherapy efficacy.^{28 29 32} Although, such macrophages display a similar transcriptional profile to their monocyte-derived counterparts under homeostatic conditions, they differ in their response to signals from the TME, resulting in distinct phenotypes and functions^{32 33} potentially explaining why the tissue-resident macrophages have a stronger impact. There is quite some transcriptional heterogeneity between the identified subsets of tissue-resident M2-like macrophages with a negative effect on clinical outcome, but a number of genes (*Cd163*, *Lyve1*, *Maf*, *Mrc1* and *Timd4*) reappear in all profiles^{25 34–36} and may form the core profile for this immune suppressive subset. At this point, it remains to be solved if all these subsets represent truly discrete populations of macrophages or whether they represent macrophages with subtle differences in their specific functional state, potentially induced by the anatomical location they reside in.

A more effective antitumor response, generated by the depletion of CD163⁺ macrophages or by vaccination strategy 2 resulted in the influx of non-classical naïve CD62L⁺CD44⁺CD27⁺ CD8⁺ T cells. Previously, these CD27⁺ naïve-like CD8⁺ T cells lack the ability to produce perforins and granzymes but did produce cytokines.^{12 37} They stimulate the formation of lymph node-like vasculature inside the tumor and as such the influx of naïve T



Literature cell type	Top 20 up- and downregulated in this study vs. literature score (out of 40)	Top 20 up- and downregulated in literature vs. this study score (out of 40)	Combined score (out of 80)
Mouse MoMac (Casanova-Acebes et al., 2021)	$16 + 7 - 2 - 5 = 16$ Overlapping Upregulated genes: Lyve1, Cd209f, Cd209g, Fcrl2, Mmp12, Arg1, Mgarp, 4930430E12rik, Cox4i2, Mmp13, Ccl7, Ccl163, Syng1, Fcna, Gdpd1, Ccl8 Overlapping Downregulated genes: Pi16, Ace, can, F5, Rab44, Cx3cl1, Cd177	$15 + 8 - 2 - 1 = 20$ Overlapping upregulated genes: C1qa, C1qb, C1qc, C1gc, Retnla, Arg1, H2-Eb1, P14, H2-Aa, H2-Ab1, Mgl2, Ccl7, Mmp12, Cxcl16, Cd74, C3ar1 Overlapping downregulated genes: Plet1, Pglyrp1, Chil3, Ear2, Il18, Serpinb1a, Cd2, Perp	36
Human MoMac (Casanova-Acebes et al., 2021)	$9 + 4 - 1 - 3 = 9$ Overlapping Upregulated genes: Lyve1, Fcrl2, Mmp12, Ch25h, Aldoc, Ccl7, Cd163, Gdpd1, Ccl8 Overlapping Downregulated genes: Vcan, F5, Rab44, Fn1	$7 + 5 - 1 - 0 = 11$ Overlapping upregulated genes: Sepp1, Mmp12, Pla2g7, Cxcl9, Lgmn, Fcrl2, Rgs1 Overlapping downregulated genes: Hp, Inhba, Mcemp1, Cpe, Serpinb2	20
Heart (Pinto et al., 2012)	$6 + 4 - 1 - 0 = 9$ Overlapping Upregulated genes: Lyve1, Fcrl2, Ch25h, Mmp13, Ccl7, Ccl8 Overlapping Downregulated genes: Ace, Vcan, F5, Cd177	$8 + 2 - 3 - 1 = 6$ Overlapping upregulated genes: Lyve1, Mmp13, Cbr2, Trnsf9, P14, Fcrl2, Igf1, Retnla Overlapping downregulated genes: Siglech, Crybb1	15
CD163 ^{hi} Tim4 ⁺ (Etzerodt et al., 2020)	$2 + 0 - 0 - 0 = 2$ Overlapping Upregulated genes: Lyve1, Syng1 Overlapping Downregulated genes: N/A	$1 + 1 - 0 - 0 = 2$ Overlapping upregulated genes: Rbm7 Overlapping downregulated genes: Chil3	4
Brain (Pinto et al., 2012)	$1 + 6 - 9 - 0 = -2$ Overlapping Upregulated genes: Syng1 Overlapping Downregulated genes: Pi16, Ace, Vcan, F5, Fn1, Cd177	$1 + 10 - 3 - 2 = 6$ Overlapping upregulated genes: Syng1 Overlapping downregulated genes: Plac8, Chil3, Ear2, S100a4, F13a1, Hp, Emilin2, Crp1, Mgst1	4
Lyve1 ^{hi} MHC-II ^{low} (Chakarov et al., 2019)	$9 + 2 - 5 - 0 = 6$ Overlapping Upregulated genes: Lyve1, Cd209f, Cd209g, Fcrl2, C6, Ccl7, Cd163, Fcna, Ccl8 Overlapping Downregulated genes: Rab44, Cx3cl1	$4 + 1 - 7 - 1 = -3$ Overlapping upregulated genes: Lyve1, Saa3, Ednrb, Fcna Overlapping downregulated genes: Nes	3
Tim4 ⁺ (Chow et al., 2021)	$2 + 1 - 1 - 1 = 1$ Overlapping Upregulated genes: Syng1, Gdpd1 Overlapping Downregulated genes: Ace	$0 + 2 - 3 - 2 = -3$ Overlapping upregulated genes: N/A Overlapping downregulated genes: Ear2, Ramp1	-2
Human CD16 ⁺ Monocytes (Casanova-Acebes et al., 2021)	$2 + 5 - 7 - 2 = -2$ Overlapping Upregulated genes: Aldoc, Gdpd1 Overlapping Downregulated genes: Ace, Vcan, Tpsab1, F5, Fn1	$2 + 4 - 5 - 2 = -1$ Overlapping upregulated genes: Lilra5, Cfp Overlapping downregulated genes: Fn1, Nupr1, Mcemp1, Inhba	-3
Mouse AM (Casanova-Acebes et al., 2021)	$4 + 10 - 13 - 4 = -3$ Overlapping Upregulated genes: Ch25h, Cox4i2, Aldoc, Gdpd1 Overlapping Downregulated genes: Pi16, Ace, Gm11651, Vcan, Apol7c, F5, Bak1, Dmkn, Fn1, Cd177	$2 + 7 - 6 - 4 = -1$ Overlapping upregulated genes: Ltc4s, Marco Overlapping downregulated genes: Pglyrp1, Ifitm6, Plac8, Gm9733, Cor2, F13a1, Eno3	-4
Human AM (Casanova-Acebes et al., 2021)	$1 + 9 - 10 - 1 = -1$ Overlapping Upregulated genes: Syng1 Overlapping Downregulated genes: Ace, Vcan, F5, Rab44, Bak1, Tnc, Ptk7, Cx3cl1, Ltf	$0 + 3 - 2 - 5 = -4$ Overlapping upregulated genes: N/A Overlapping downregulated genes: G0s2, Gpr183, Ereg	-5
Human CD14 ⁺ Monocytes (Casanova-Acebes et al., 2021)	$6 + 4 - 5 - 9 = -4$ Overlapping Upregulated genes: Mgarp, Ch25h, Cox4i2, Aldoc, Syng1, Gdpd1 Overlapping Downregulated genes: Ace, Tpsab1, Bak1, Fn1	$3 + 2 - 7 - 7 = -9$ Overlapping upregulated genes: Cd300e, Cfp, Serpin9 Overlapping downregulated genes: Nupr1, Fn1	-13
Mouse pMono (Casanova-Acebes et al., 2021)	$0 + 10 - 18 - 4 = -12$ Overlapping Upregulated genes: N/A Overlapping Downregulated genes: Vcan, Apol7c, F5, Rab44, Gm16194, Cx3cl1, Dmkn, Fn1, Cd177, Ltf	$3 + 3 - 5 - 9 = -8$ Overlapping upregulated genes: Cd300e, Cd300d, Hfe Overlapping downregulated genes: Plet1, F13a1, Chil3	-20
Spleen (Pinto et al., 2012)	$0 + 0 - 10 - 2 = -12$ Overlapping Upregulated genes: N/A Overlapping Downregulated genes: N/A	$4 + 1 - 9 - 10 = -14$ Overlapping upregulated genes: Apol7c, Serpina3g, Gbp8, Apol7c Overlapping downregulated genes: Tjp1	-26
Mouse Inf. Monocytes (Casanova-Acebes et al., 2021)	$0 + 4 - 18 - 8 = -22$ Overlapping Upregulated genes: N/A Overlapping Downregulated genes: Ace, Gm15564, Rab44, Cx3cl1	$1 + 1 - 8 - 11 = -17$ Overlapping upregulated genes: Saa3 Overlapping downregulated genes: Plet1	-39

Figure 8 CD163^{hi} macrophages resemble M2 macrophages in humans and are of a tissue-resident nature. Comparison of the transcriptome profile of CD163^{hi} macrophages from this study to 14 established monocyte and macrophage types from literature. Maximum similarity scores to the CD163^{hi} macrophages (max. 40; left column) were combined with maximum similarity score to the literature cell types (max. 40; right column), resulting in a maximum combined score of 80 (right column). When a particular gene from the top 20 was also present in the top 20% DEG from the corresponding gene set, this gene was written in bold. An example of the scoring system is shown in the green box.

cells that are locally activated to become fully functional effector cells.^{38–40} This leaves us to speculate that in the absence of CD163⁺ macrophages, intratumoral priming of T cells occurs, a process which may contribute to the overall efficacy of immunotherapy.

RNA sequencing allowed us to identify three main pathways enriched in the CD163^{hi} tissue-resident macrophages: blood vessel development, ECM remodeling, and wound healing. A tissue-resident macrophage subset with a phenotypic signature similar to the CD163^{hi} macrophages has been found in the arterial wall and the adult heart.^{41–42} Additionally, Lyve1⁺ macrophages were shown to control vessel permeability and density.^{43–44} Interestingly, cardiac macrophages with an M2-like phenotype have been indicated as excellent regulators of ECM remodeling.^{45–46} Reorganization of the ECM contributes to tumor progression and therapy resistance,^{47–48} and is tightly interwoven with the wound healing process, for which CD163⁺ macrophages are well known.^{49–50} We and others showed that CD163⁺ tissue-resident macrophages in tumors have a strong anti-inflammatory wound healing signature, specifically through high *Hmox1* expression.^{35–51–52} CD163 is the receptor for the hemoglobin/haptoglobin complex and these cells thus are by default involved in the degradation of heme, resulting in the local release of the anti-inflammatory factors iron, biliverdin and carbon oxide.^{23–53} It is therefore not surprising that many attempts to inhibit tumor growth through the blockade of this pathway have been undertaken, with promising preclinical results.^{54–56} CD163-depletion as well as HO-1 inhibition resulted in similar phenotypic changes of CD8⁺ T cells in the TME. Therefore, the downstream effects of HO-1 forms one mechanism employed by CD163^{hi} macrophages to suppress CD8⁺ T cell activity. Importantly, CD163^{hi} macrophages also showed increased expression of Arg1, Ido1 and IL-10, three other pathways known to suppress the function of CD8⁺ T cells in tumors.⁵⁷ It is very likely that these pathways also played a role in CD163^{hi} macrophage-mediated inhibition of CD8⁺ T cells in our tumor models. As these immune suppressive pathways are well established and known to be used by other subsets of immune suppressive cells too, we focused our attention on the role of *Hmox1* in this manuscript, as this enabled us to establish a direct link between gene expression and function of the macrophages in the suppression of CD8⁺ T cells. Interestingly, interference with only one of the inhibitory mechanisms (HO-1) employed by CD163^{hi} macrophages can already shift the balance in the TME towards tumor control, which is in line with checkpoint inhibition, where despite the expression of multiple co-inhibitory molecules on activated CD8⁺ T cells, blockade of one such a molecule can have dramatic improvement of clinical outcome.

Earlier studies showed that the number of tumor-infiltrating macrophages, independent of their phenotype, is associated with poor clinical outcome.^{30–58} Hence, targeting of pathways that interfered with their recruitment, activation or polarization have been proposed as

potential therapeutic strategies.⁵⁹ Strategies to prevent the recruitment are of no use when it comes to tissue-resident macrophages.³² Targeting of the Csf1/Csf1r axis, a signaling pathway that plays an essential role in differentiation and maintenance of most macrophage populations, has been studied in the clinic based on preclinical data showing a delay in tumor outgrowth in different tumor models.^{60–63} Yet, a series of clinical trials targeting the Csf1/Csf1r axis have met with limited results.⁶⁴ We demonstrated that the CD163^{hi} population is less sensitive to Csf1r inhibition when compared with the majority of other macrophage populations. This not only suggests a cellular maintenance pathway independent of Csf1/Csf1r signaling active in CD163^{hi} macrophages but also may explain why blockade of this signaling axis has limited clinical potential. In addition, the depletion not only of tumor-supporting but also of the tumor-rejecting macrophages that are required to achieve tumor regression may also underly the disappointing clinical outcomes.^{11–65–66} Indeed, we showed that the treatment with the Csf1r inhibitor PLX3397 results not only in the decrease of macrophages but also in that of several other myeloid cell populations and completely abolished the clinical effect of therapeutic vaccination in the TC-1 tumor model, while targeting of the CD163⁺ macrophage population allowed a full immune-mediated tumor regression and prevented secondary resistance. The size and phenotype of the tumor-rejecting macrophage pool is still elusive but attempts to stimulate their killing and phagocytic capacity by targeting myeloid cell checkpoints are currently undertaken.^{67–69} Notably, our observation that a Csf1r⁺ macrophage is positively associated with therapy success was recently confirmed in patients with non-small cell lung cancer on immune checkpoint therapy.²⁹ Together with our new data, this illustrates that within the same tumor at least two distinct macrophage populations are present. A Csf1r⁺ subset, of pivotal importance for therapy-induced tumor control, and a Csf1r⁻ subset that dictates immunotherapy resistance. These findings underline the clinical importance of selective macrophage targeting strategies.

In general the expression of CD163 on the surface of macrophages is believed to be a strong indicator of an anti-inflammatory and tissue-resident phenotype. Indeed, here, we show that a small tissue resident CD163⁺ macrophage population at the invasive margin of the tumor is responsible for both primary and secondary resistance against cancer immunotherapy. In line with this, the presence of a small subset of CD163⁺ macrophages at the invasive front was associated with tumor progression in colorectal cancer, as well as resistance to BCG-immunotherapy in bladder cancer,^{70–71} suggesting that these macrophages may act on CD8⁺ T cells before they enter the tumor cell nests. This would fit with our observation that both the depletion of CD163 macrophages and the inhibition of HO-1 results in a more prominent presence of non-classically activated naïve T cells in the tumor, indicative for a change in the capacity of new T cells to infiltrate the tumor. A similar ‘gate-keeper’

function has been reported for Tim-4⁺ cavity-resident macrophages in NSCLC.³⁴ Additionally, the expression of CD163 is not limited to M2 tissue-resident macrophages per se^{18,19} and, therefore, may not always identify the tumor-promoting macrophage population. In addition, whereas the lack or low Csf1r expression by such CD163⁺ macrophages has, similar to our study, been associated with resistance to immunotherapy²⁹ the expression of PD-L1 by CD163⁺ macrophages was not.^{29,72} Therefore, we suggest to use CD163 in combination with at least one other functional marker, such as Lyve1, CD206, c-Maf, or Tim4. These and other markers found to be upregulated on the CD163^{hi} macrophage population in this study, are involved in tumor progression and in the response to therapy in human cancers.^{17,27–29,34,36,72}

Finally, the heterogeneity between CD163⁺ macrophage subtypes, a feature for which macrophages are notorious, is associated with a high diversity in the genes of tumor-supporting pathways (eg, HO-1, Arginase, IL-10) enriched in these CD163⁺ tissue-resident macrophages.^{14,35} This suggests that it is more efficacious to deplete these macrophages at the cellular level, rather than targeting one or more downstream pathways.

MATERIALS AND METHODS

Experimental design

Mice

C57BL/6J (BL/6J) mice were obtained from Charles River Laboratories (France), TCR transgenic mice containing gp100_{25–33}/H-2D^b-specific receptors were bred to express the congenic marker CD45.1 (Ly5.1) and were a kind gift from Dr. N.P. Restifo (NIH, Bethesda, USA). All animals were housed in individually ventilated cages under specified pathogen-free conditions in the animal facility of the Leiden University Medical Center. Female and male BL/6 J mice of 8–10 weeks of age at the start of the experiment were used for the TC-1 and RMA-Qa1^{-/-} model, respectively. Male Ly5.1 mice aged 8–12 weeks were used for RMA-Qa1^{-/-} TME studies. Animals were subcutaneously inoculated with 1 × 10⁵ TC-1, 1 × 10³ RMA-Qa1^{-/-} or 1 × 10⁵ KPC3 tumor cells in 100 μL Phosphate Buffered Saline (PBS) containing 0.1% bovine serum albumin (BSA) on day 0 in the right, or right and left flank. Tumor volume (l × w × h) was measured thrice weekly using a caliper. Animals were randomized prior to treatment and experimental measurements were conducted in a blinded manner.

Tumor cell lines

TC-1 serves as model for HPV-induced cancer and was generated by the transduction with the E6 and E7 oncoproteins of HPV16.⁷³ RMA-Qa1^{-/-} is a Raucher MuLV-induced T cell lymphoma RBL-5 cell line, generated by the CRISPR-Cas9-induced knock out of the Qa-1^b gene. For the establishment of a homogenous Qa1^b knockout cell line, cells were incubated for 48 hours with 30 IU/mL IFN-γ (Biological) and subsequently FACS sorted three

times on Qa1^b- cells.¹³ KPC3 is a derivate cell line of a KPC tumor with mutant *p53* and *K-ras*.⁷⁴ TC-1, RMA-Qa1^{-/-} and KPC3 are all BL/6J mouse-derived tumor cell lines. Cell lines were cultured in Iscove's modified Dulbecco's medium (IMDM; Invitrogen) supplemented with 8% Fetal Calf Serum (FCS; Greiner), 100 IU/mL Penicillin/Streptomycin (Gibco) and 2 mM glutamin (Gibco) at 37°C and 5% CO₂. TC-1 cells were additionally supplemented with 400 μg/mL Neomycin (G418), 1x MEM non-essential amino acids (Gibco) and 1 mM Sodium Pyruvate (Life Technologies). A low and constant passage number was used in all experiments. Cell lines were regularly assured to be Mycoplasma and rodent virus negative by PCR analysis. Authentication of the cell lines was done by antigen-specific T cell recognition.

Method details

Treatment

All tumor treatments were randomized based on tumor volume and given in a blinded manner. Tumor treatment graphics and timelines were created with BioRender. Mice-bearing TC-1 tumors were treated with a SLP vaccination when tumors reached a size of 50–100 mm³. The SLP vaccine, containing 100 μg HPV16 E7_{43–63} (GQAE PDRAHYNIVTFCKKCD) peptide, supplemented with 20 μg CpG (ODN1826, InvivoGen) was dissolved in 200 μL PBS emulsified with Freund's adjuvants and administered subcutaneously in the contralateral flank for vaccination strategy 1 or dissolved in 50 μL PBS and administered subcutaneously in the tail base for vaccination strategy 2. Mice-bearing RMA-Qa1^{-/-} tumors were treated with therapeutic vaccination when tumors reached a size of 10–50 mm³. The peptide vaccine, containing 50 nmol of the Gag-encoded CD8 T cell epitope (CCLCLTVFL) and 20 nmol of the murine leukemia virus Env-encoded CD4 T cell epitope (EPLTSLTPRCNTAWNRLKL), supplemented with 20 μg CpG (ODN1826, InvivoGen) was dissolved in 50 μL PBS, and administered subcutaneously in the tail base. CD115⁺ macrophages were depleted from day 8 after tumor inoculation by the Csf1r kinase and c-Kit inhibitor PLX3397 (Plexxikon), incorporated into rodent chow diet at 275 mg/kg (daily dose ~45 mg/kg) and compared with control chow diet. Treatment with αCD163-DXR or αCD163-Ctrl liposomes was started 1 day after therapeutic vaccination and administered every other day with a total of 3–4 injections. Liposomes were administered by retro-orbital injection during isoflurane-induced anesthesia. HO-1 activity was blocked by intraperitoneal injection of 5 mg/kg Tin Protoporphyrin IX dichloride (SnPP) in 0.1N NaOH (Merck) in PBS pH7.5. Treatment with SnPP was started 1 day after therapeutic vaccination and continued three times per week for the duration of the study. KPC3 tumor-bearing animals were untreated and sacrificed at day 21 after tumor inoculation. For all treatments no adverse effects were observed. Animals were euthanized when tumors reached a size of 1000 mm³ (unilateral model) or a combined volume of 1500 mm³ (bilateral model).

Flow cytometry

For TME studies, mice were euthanized at indicated time points and tumors were collected for flow cytometry analysis. Tumors with a size $>36 \text{ mm}^3$ were included and minced using razor blades, followed by chemical digestion with Liberase TL (2.5 mg/mL, Roche) for 10 min at 37°C . Tumors were further processed into single-cell suspensions by using $70 \mu\text{m}$ cell strainers (BD Biosciences) and resuspended in PBS. Mouse Fc-receptors were blocked by Rat Anti-Mouse CD16/CD32 (Clone 2.4G2, BD) for 15 min at 4°C . Viability was assessed with the Zombie UV Fixable Viability Kit (Biolegend) or the LIVE/DEAD Fixable Aqua Dead Cell Stain Kit in PBS before surface staining. Qa1^b staining was performed with biotin-labeled anti-Qa1^b in PBS supplemented with 0.5% BSA+0.02% Sodium azide (FACS buffer) followed by streptavidin-APC staining in FACS buffer, both for 30 min at 4°C . APC-conjugated HPV16 E7₄₉₋₅₇ tetramers (RAHYNIVTF) were added to the surface staining mix. Surface staining was performed in FACS buffer for 20 min at 4°C . Subsequently, cells were fixed and permeabilized for intracellular marker staining using the FoxP3/Transcription Factor Staining Buffer Set (eBioscience) according to manufacturer's protocol. Following intracellular staining, cells were resuspended in FACS buffer and acquired on the Aurora 5 L spectral flow cytometer (Cytek) or the LSR-II (BD Biosciences). Data were analyzed using FlowJo (Tree Star) for the analysis of cellular and percentages or OMIQ data analysis software for the visualization of opt-SNE plots.⁷⁵

Immunohistochemistry

Tumors and organ tissue were isolated from mice and directly fixed in formalin, followed by embedding in paraffin. Tumor and organ tissues were sliced into $4 \mu\text{m}$ sections and mounted on adhesive slides. Sections were then deparaffinized and rehydrated after which endogenous peroxidase activity was blocked with 0.3% hydrogen peroxidase solution (Merck Millipore) in methanol for 20 min. For F4/80 staining, antigen retrieval was performed in preheated Trypsin solution (Trypsin 1%+CaCl₂ 1% in H₂O, pH 7.4) at 37°C for 30 min. For CD163, CD31, HO-1 and CD8 staining, antigen retrieval was performed in 0.01M Sodium Citrate solution (Merck Millipore, pH 6.0) in the microwave for 10 min. Non-specific binding of the primary antibody was reduced by SuperBlock (PBS) Blocking Buffer (ThermoFisher) at room temperature for 30 min. Tumor or organ slides were incubated with rat anti-mouse F4/80 (clone CI:A3-1, Sanbio), rat anti-mouse CD8 (clone 4SM15, eBioscience), rabbit anti-mouse CD163 (clone M-96, Santacruz), goat anti-mouse CD31 (clone M-20, Santacruz), or rabbit anti-heme oxygenase 1 (clone EPR18161-128, Abcam) antibodies diluted in 1% BSA in PBS at 4°C overnight. Slides were then washed (0.05% Tween in PBS) and incubated with biotinylated Rabbit anti-rat IgG (Abcam), goat anti-rabbit IgG (Agilent) or Rabbit anti-goat IgG (Agilent) respectively, at room temperature for 1 hour. Biotinylated

antibodies were labeled using the VECTASTAIN Elite ABC-HRP Kit (Vetorlabs) according to manufacturer's protocol. Nuclear counterstaining was performed with filtered Mayer's Haematoxylin staining (ThermoFisher) at room temperature for 10–15 s. Antibody binding was detected with the Liquid DAB⁺ substrate chromogen system (DAKO, Agilent) and percentage DAB staining was quantified using ImageJ software. For the detection of collagen, slides were stained using the Masson's Trichrome Stain Kit according to protocol. In short, staining was performed in preheated Bouin's Fixative for 1 hour, Weigert's Iron Hematoxylin Working Solution for 10 min and Biebrich Scarlet—Acid Fuchsin Solution for 5 min, respectively. Subsequently, slides were transferred to phosphotungstic/phosphomolybdic acid for 10 min, Aniline Blue for 30 min and Acetic acid for 1 min prior to dehydration and mounting of cover slides. On all immunohistochemistry pictures in this paper a photo correction of +200% saturation, -20% brightness and +40% contrast was applied.

RNA sequencing

For bulk RNA sequencing, mice-bearing TC-1 tumors were treated with SLP vaccination in the tail base when tumors were $50\text{--}100 \text{ mm}^3$. At time of regression, tumors were harvested and processed into single cell suspensions as described above. From single cell suspensions CD163^{hi}, CD163^{dim} and CD163^{lo} macrophages were sorted using the BD Aria cell sorter and collected at a purity of 80%–95%. RNA from CD163^{hi}, CD163^{dim} and CD163^{lo} macrophages was isolated using the NucleoSpin Mini Kit for RNA Purification according to protocol.

Sample quality control and bulk RNA sequencing were both performed by GenomeScan (Leiden, The Netherlands). Sample preparation was performed using the NEBNext Low Input RNA Library Prep Kit for Illumina according to protocol (NEB #E6420S/L). The quality and yield after sample preparation were determined using the Agilent DNF-474 HS NGS Fragment Kit and measured with the Fragment Analyzer. The size of the resulting products was consistent with the expected size distribution with a peak between 200 and 400 bp. The presence of ribosomal, globin and mitochondrial content was determined for all samples as an additional quality check. An input concentration of 1.1 nM of DNA was used. Clustering and DNA sequencing using the NovaSeq6000 was performed according to manufacturer's protocols. For each sample, the trimmed reads were mapped to the mouse GRCm38.p6 (Mus_musculus.GRCm38.dna.fa) reference sequence using a short read aligner based on Burrows-Wheeler Transform (Tophat v2-2.1) with default settings. Frequency of unique mapped reads within exon regions was determined with HTSeq V.0.11.0. Read counts were used to compare CD163^{hi} with CD163^{dim} and CD163^{lo} macrophages in the R package DESeq2 V.2.1.14. From this the Log₂ fold change (FC) and the adjusted p value were determined for the differentially expressed (DE) genes. Image analysis, base calling, and quality check was

Table 1 Available datasets for the comparison of the CD163^{hi} gene signature to established monocyte and macrophage types from literature

Cohort	Cell type	Species	Data source
34	Tim4 ⁺ vs Tim4 ⁻ steady state cavity macrophages	Mouse	Supplementary
25	CD163 ⁺ Tim4 ⁺ vs CD163 ⁺ Tim4 ⁻ macrophages (10 weeks)	Mouse	E-MTAB-8141
44	Lyve1 ^{hi} MHCII ^{lo} vs Lyve1 ^{lo} MHCII ^{hi}	Mouse	Provided by Chakarov, S.
27	Alveolar Macrophages (AM), Monocyte/Macrophages (MoMac), pMonocytes (pMono), Infl. Monocytes	Mouse	Supplementary
27	AM, MoMac, CD14 ⁺ Monocytes, CD16 ⁺ Monocytes	Human	Supplementary
42	Macrophages from heart, brain and spleen	Mouse	Supplementary

performed with the Illumina data analysis pipeline RTA V.3.4.4 and Bcl2fastq V.2.20.

The resulting genes of the DE analysis were used in a GSEA of Gene Ontology using the gseGO function in R studio (clusterProfiler package V.4.0.5, R V.4.1.0, R studio V.1.4.1717). Redundant GO terms were removed from the found GO terms (adjusted p<0.05, 251 total) of the gseGO result using the REViGO tool, available at <http://revigo.irb.hr/>. GO terms were entered with corresponding adjusted p values and selected settings for redundancy removal were 'small' with the 'SimRel' semantic similarity measure using the Mus Musculus database. Reduced GO terms were visualized using Cytoscape (V.3.8.2) where GO terms were plotted in a circular layout.

In order to compare the CD163^{hi} gene signature from this study to established monocyte and macrophage types from literature, DE genes with adjusted p value <0.05 were collected from available datasets (table 1) and classified as upregulated (log₂FC>0) or downregulated (log₂FC<0). In the case of E-MTAB-8141 (P1 vs P2), we reproduced the differential gene expression analysis following the description in.²⁵ We then compared this list of with upregulated and downregulated genes (log₂FC>0 and log₂FC<0 respectively, adjusted p value <0.05) from our cohort (CD163^{hi} macrophages). Additionally, we defined a CD163^{hi} gene set composed of the top 20 enriched genes from the CD163^{hi} macrophages together with *Hmox1* and *Maf*. This gene set was then compared with the cellxgene MoMac_VERSE human dataset of different monocyte and macrophage populations from cancer and healthy tissue.

SnPP in vitro assay

To assess the effect of the HO-1 inhibitor Tin Protoporphyrin IX dichloride (SnPP) on T cells, 5×10⁶ splenocytes from naïve mice were cultured with 20 IU/mL IL-2 in 24-well flat-bottom culture plates and activated with CD3/CD28 dynabeads (ThermoFisher). Splenocytes were then exposed to 0, 50 or 100 µM SnPP in 0.1N NaOH (Merck) in PBS pH7.5. After 48 hours, the phenotype of splenocytes was established by spectral flow cytometry.

Quantification and statistical analysis

All experiments were performed with a minimum of four biological replicates. A priori sample size calculation based on expected median survival times or percentages of infiltrating immune cells was used to determine the required number of animals for each experiment. Statistical significance between two groups was determined using an unpaired two-tailed Student's t-test and between >2 groups using a one-way analysis of variance with Bonferroni's correction for multiple comparisons. For survival analyses, a logrank Mantel-Cox test and for response rates a Mann-Whitney U test were performed. All statistical tests were performed using the GraphPad Prism software (V.9). Statistical methods can be found in the figure legends or tables. Data are represented as the mean±SEM unless stated otherwise. Statistical significance is shown as * = p<0.05, ** = p<0.01, *** = p<0.001 and ****<0.0001.

Key resources table

Reagent or Resource	Source	Identifier
Antibodies		
Purified CD16/CD32 (2.4G2)	BD Biosciences	Cat#: 553141; RRID: AB_394656
4-1BB – APC (17B5)	Biolegend	Cat#: 106110; RRID: AB_2564297
Arg-1 – PE/Cy7 (A1exF5)	Invitrogen	Cat#: 25-3697-82; RRID: AB_2734841



Reagent or Resource	Source	Identifier
CCR2 – BV785 (SA203G11)	Biolegend	Cat#: 150621; RRID: AB_2721565
CD3e – FITC (145–2 C11)	Invitrogen	Cat#: 11-0031-85; RRID: AB_464883
CD3e – PE/Cy5 (145–2 C11)	Biolegend	Cat#: 100310;
CD3e – BV510 (145–2 C11)	BD Biosciences	RRID: AB_312675 Cat#: 563024; RRID: AB_2737959
CD4 – BUV496 (RM4-5)	BD Biosciences	Cat#: 741050; RRID: AB_2870665
CD8a – BUV395 (53–6.7)	BD Biosciences	Cat#: 565968; RRID: AB_2739421
CD11b – BUV563 (M1/70)	BD Biosciences	Cat#: 741242;
CD11b – APC/Fire750 (M1/70)	Biolegend	RRID: AB_2870793 Cat#: 101262; RRID: AB_2572122
CD11c – BV605 (HL3)	BD Biosciences	Cat#: 563057;
CD11c – APC/Fire750 (N418)	Biolegend	RRID: AB_2737978 Cat#: 117352; RRID: AB_2572124
CD19 – SparkBlue550 (6D5)	Biolegend	Cat#: 115566;
CD19 – BV510 (1D3)	BD Biosciences	RRID: AB_2832389 Cat#: 562956; RRID: AB_2737915
CD24 – BV650 (M1/69)	BD Biosciences	Cat#: 563 545 RRID: AB_2738271
CD25 – BV421 (PC61)	Biolegend	Cat#: 102043; RRID: AB_2562611
CD27 – BUV785 (LG.3A10)	Biolegend	Cat#: 124241; RRID: AB_2800595
CD28 – PE/Cy7 (37.51)	Biolegend	Cat#: 102126; RRID: AB_2617011
CD39 – PE (Duha59)	Biolegend	Cat#: 143804; RRID: AB_11218603
CD44 – BV510 (IM7)	Biolegend	Cat#: 563114;
CD44 – BV785 (IM7)	Biolegend	RRID: AB_2738011 Cat#: 103 059 RRID: AB_2571953
CD45 – AlexaFluor700 (30-F11)	Biolegend	Cat#: 103128; RRID: AB_493715
CD45.1 – AlexaFluor700 (A20)	Biolegend	Cat#: 110724; RRID: AB_493733
CD45.2 – FITC (104)	Biolegend	Cat#: 109 806 RRID: AB_313443
CD47 – APC/Cy7 (miap301)	Biolegend	Cat#: 127 526 RRID: AB_2632862
CD49a – BUV737 (Ha31/8)	BD Biosciences	Cat#: 741776; RRID: AB_2871130
CD54 – FITC (YN1/1.7.4)	ThermoFisher	Cat#: 11-0541-82 RRID: AB_465094
CD62L – BUV805 (MEL-14)	BD Biosciences	Cat#: 741924; RRID: AB_2871237
CD69 – BUV737 (H1.2F3)	BD Biosciences	Cat#: 612793; RRID: AB_2870120
CD86 – BUV496 (PO3)	BD Biosciences	Cat#: 750437; RRID: AB_2874600

Reagent or Resource	Source	Identifier
CD106 – PE (429)	Biologend	Cat#: 105 714 RRID: AB_1134164
CD115 – PE/Dazzle594 (AFS98)	Biologend	Cat#: 135528; RRID: AB_2566523
CD122 – PE/Cy5 (TM-β1)	Biologend	Cat#: 123220; RRID: AB_2715962
CD163 – BV421 (S15049I) CD163 – APC (S15049I)	Biologend Biologend	Cat#: 155309; RRID: AB_2814063 Cat#: 155 306 RRID: AB_2814060
CTLA-4 – BV421 (UC10-4B9)	Biologend	Cat#: 106312; RRID: AB_2563063
Egr2 – APC (Erongr2)	Invitrogen	Cat#: 17-6691-82; RRID: AB_11151502
Eomes – PE/eFluor610 (Dan11mag)	Invitrogen	Cat#: 61-4875-82; RRID: AB_2574614
F4/80 – PE/Cy5 (BM8) F4/80 – PE (Qa17A29)	Biologend Biologend	Cat#: 123112; RRID: AB_893482 Cat#: 157 304 RRID: AB_2832547
FoxP3 – PacificBlue (MF-14)	Biologend	Cat#: 126410; RRID: AB_2105047
Gata-3 – AlexaFluor488 (TWAJ)	Invitrogen	Cat#: 53-9966-42; RRID: AB_2574493
Granzyme B – PerCP-Cy5.5 (QA16A02)	Biologend	Cat#: 372212; RRID: AB_2728379
IFN γ – PE/Cy7 (XMG1.2)	BD Biosciences	Cat#: 557649; RRID: AB_396766
IL-2 – PE (JES6-5H4)	Biologend	Cat#: 503808; RRID: AB_315302
iNOS – AlexaFluor488 (CXNFT)	Biologend	Cat#: 53-5920-82; RRID: AB_2574423
Ki-67 – BV605 (16A8)	Biologend	Cat#: 652413; RRID: AB_2562664
KLRG1 – PerCP/Cy5.5 (2F1/KLRG1)	Biologend	Cat#: 563595; RRID: AB_2738301
Ly6C – PerCP/Cy5.5 (HK1.4)	Biologend	Cat#: 128012; RRID: AB_1659241
Ly6G – SparkBlue550 (1A8) Ly6G – APC/Fire750 (1A8)	Biologend Biologend	Cat#: 127664; RRID: AB_2860671 Cat#: 127652; RRID: AB_2616733
I-A/I-E – PacificBlue (M5/114.15.2)	Biologend	Cat#: 107620; RRID: AB_493527
NK1.1 – BV650 (PK136) NK1.1 – BV510 (PK136)	BD Biosciences Biologend	Cat#: 564143; RRID: AB_2738617 Cat#: 108738; RRID: AB_2562217
NKG2A – PE/Cy7 (16A11)	Biologend	Cat#: 142810; RRID: AB_2728161
OX-40 (CD134) – BV711 (OX-86)	Biologend	Cat#: 119421; RRID: AB_2687176
PD-1 – BV605 (29F.1A12)	Biologend	Cat#: 135220; RRID: AB_2562616



Reagent or Resource	Source	Identifier
PD-L1 – BUV737 (MIH5)	BD Biosciences	Cat#: 741877; RRID: AB_2871203
Qa1 ^b – Biotin (6A8.6F10.1A6)	BD Biosciences	Cat#: 559 829 RRID: AB_397345
RORγT – PE (AFKJS-9)	Invitrogen	Cat#: 12-6988-82; RRID: AB_1834470
Siglec-F – BV711 (E50-2440)	BD Biosciences	Cat#: 740764; RRID: AB_2740427
Siglec-G – BUV615 (SH1)	BD Biosciences	Cat#: 751581; RRID: AB_2875576
Siglec-H – BV650 (440 c)	BD Biosciences	Cat#: 747672; RRID: AB_2744233
SIRPα – APC/Cy7 (P84)	Biolegend	Cat#: 144018; RRID: AB_2629558
T-bet – BV711 (4B10)	Biolegend	Cat#: 644820; RRID: AB_2715766
TCF1/7 – AlexaFluor647 (812145)	R&D Systems	Cat#: FAB8224R; RRID: AB_2888931
TIGIT – PE/Dazzle594 (1G9)	Biolegend	Cat#: 142110; RRID: AB_2566573
Tim-3 – BV785 (RMT3-23)	Biolegend	Cat#: 119725; RRID: AB_2716066
TNF-α – APC/Cy7 (MP6-XT22)	Biolegend	Cat#: 506344; RRID: AB_2565953
XCR1 – PE (ZET)	Biolegend	Cat#: 148204; RRID: AB_2563843
HPV16 E7 ₄₉₋₅₇ – APC (RAHYNIVTF)	Peptide synthesis facility of department IHB, LUMC	N/A
Rat anti-mouse F4/80 (Cl:A3-1)	Sanbio	Cat#: MCA497; RRID: AB_2098196
Rat anti-mouse CD8 (4SM15)	eBioscience	Cat#: 14-0808-82 RRID: AB_2572861
Rabbit anti-rat IgG	Abcam	Cat#: ab6733; RRID: AB_954909
Rabbit anti-mouse CD163 (M-96)	Santacruz	Cat#: sc-33560; RRID: AB_2074556
Goat anti-rabbit IgG	Agilent	Cat#: E0432; RRID: AB_2313609
Goat anti-mouse CD31 (M-20)	Santacruz	Cat#: sc-1506 RRID: AB_2161037
Rabbit anti-Heme Oxygenase 1 (EPR18161-128)	Abcam	Cat#: ab237267 RRID: AB_764541
Rabbit anti-goat IgG	Agilent	Cat#: P0449 RRID: AB_2617143
APC Goat Anti-Rat Ig	BD Biosciences	Cat#: 551 019 RRID: AB_398484
Streptavidin – APC	eBioscience	Cat#: 17-4317-82
Mouse T-Activator CD3/CD28 Dynabeads	ThermoFisher	Cat#: 11-452-D
Chemicals, peptides, and recombinant proteins		
Lipofectamine 2000 Transfection Reagent	Invitrogen	Cat#: 11 668 027
Recombinant IFN-γ	Biolegend	Cat#: 575 308
Recombinant IL-2	Peptotech	Cat#: 212-12

Reagent or Resource	Source	Identifier
Zombie UV fixable viability kit	Biologend	Cat#: 423 108
LIVE/DEAD Fixable Aqua Dead Cell Stain Kit	ThermoFisher	Cat#: L34957
Liberase TL Research grade	Roche	Cat#: 05401020001
FoxP3/Transcription Factor Staining Buffer Set	Invitrogen	Cat#: 00-5523-00
HPV16 E7 ₄₃₋₆₃ peptide (GQAEPDRAHYNIVTFCKCDS)	Peptide synthesis facility of department IHB, LUMC	N/A
RMA Env-encoded CD4 T cell epitope (EPLTSLTPRCNTAWNRLKL)	Peptide synthesis facility of department IHB, LUMC	N/A
RMA Gag-encoded CD8 T cell epitope (CCLCLTVFL)	Peptide synthesis facility of department IHB, LUMC	N/A
CpG (ODN 1826)	Invivogen	Cat#: tlr1-1826
Incomplete Freund's Adjuvant (Difco)	BD Biosciences	Cat#: 263 910
PLX3397 275 mg/kg rodent chow diet	Research Diets Inc.	N/A
Control rodent chow diet	Research Diets Inc.	N/A
αCD163-DXR liposomes ⁽¹⁵⁾ αCD163-Control liposomes ⁽¹⁵⁾	Department of Biomedicine, University of Aarhus	N/A
Tin Protoporphyrin IX dichloride	Santa Cruz Biotechnology	Cat#: sc-203452B
Entellan mounting medium for microscopy	Sigma Aldrich	Cat#: 107 960
PAP pen for immunostaining	Merck Millipore	Cat#: Z377821
Microscope slides, SuperFrost Plus	VWR	Cat#: 631-0108
Hirschmann Glass covers	ThermoFisher	Cat#: 10 329 241
Hydrogen peroxide 30%	Merck Millipore	Cat#: 107 209
Methanol>98.5%	VWR Chemicals	Cat#: 20 903.415
Trypsin powder	Merck	Cat#: 85 450C
Calcium Chloride	Merck	Cat#: 793 639
Tri-sodium Citrate Dihydrate	Merck	Cat#: 106 448
SuperBlock (PBS) Blocking Buffer	ThermoFisher	Cat#: 37 515
Bovine Serum Albumin (BSA)	Sigma Aldrich	Cat#: A3912
Tween 20	Merck	Cat#: 8221840500
VECTASTAIN Elite ABC-HRP Kit	Vectorlabs	Cat#: PK-6100; RRID: AB_2336819
Mayer's haematoxylin staining	Merck	Cat#: 1092490500
DAB ⁺ Substrate Chromogen System (Dako Omnis)	Agilent	Cat#: GV825
Masson's Trichrome Stain Kit	Polysciences	Cat#: 25 088
Machery-Nagel NucleoSpin RNA, Mini Kit For RNA Purification	Bioké	Cat#: 740 955.50
NEBNext Single Cell/Low Input RNA Library Prep Kit for Illumina	New England Biolabs Inc.	Cat#: E6420S
Agilent DNF-474 HS NGS Fragment Kit	Agilent	Cat#: DNF-474-0500
Deposited data		
Bulk RNAseq	Available on acceptance	N/A
Experimental models: Cell lines		
TC-1	Provided by Prof. T.C. Wu (John Hopkins University, Baltimore, U.S.A.)	RRID: CVCL_4699
RMA	Provided by Prof. K. Kärre (Karolinska Institute, Stockholm, Sweden)	RRID: CVCL_J385
KPC3	⁽⁷⁶⁾	RRID: CVCL_A9ZK

Reagent or Resource	Source	Identifier
Experimental models: Organisms/strains		
Mouse C57BL/6J	Charles River Laboratories France	N/A
Mouse TCR transgenic gp100 ₂₅₋₃₃ /H-2D ^b bred to express congenic marker CD45.1 (Ly5.1)	Provided by Dr. N.P. Restifo (NIH, Bethesda, USA)	N/A
Software and algorithms		
FlowJo V.10	Treestar	RRID: SCR_008520; https://www.flowjo.com/solutions/flowjo
OMIQ	Omiq Inc.	https://www.omiq.ai/
GraphPad Prism V.9	GraphPad	RRID: SCR_002798; http://www.graphpad.com/
ImageJ	ImageJ	RRID: SCR_003070; https://imagej.net/
R V.4.1.0	R	RRID: SCR_001905; http://www.r-project.org/
R studio V.1.4.1717	R Studio	https://www.rstudio.com/
REViGO tool	REViGO	RRID: SCR_005825; http://revigo.irb.hr/
Cytoscape V.3.8.2	Cytoscape	RRID: SCR_003032; http://cytoscape.org/
BioRender	BioRender	RRID: SCR_018361; http://biorender.com/
Cellxgene MoMac_VERSE v2021	cellxgene	RRID: SCR_021059; https://macroverse.gustaveroussy.fr/2021_MoMac_VERSE/

Acknowledgements We thank our colleagues including Christianne Groeneveldt, Jim Middelburg and Gaby Schaap for material and experimental help. We thank Gitte Fynbo Biller from the department of Biomedicine at the Aarhus University for the production of the α CD163-DXR and Control nanoparticles.

Contributors Conceptualization: SHvdB and TVH. Methodology: MJvE, CL, TVH and SHvdB. Validation: MJvE and CL. Formal Analysis: MJvE, CL JJcVST and PC. Investigation: MJvE and CL. Resources: AE. Writing: MJvE and SHvdB. Visualization: MJvE, CL and JJcVST. Supervision: TVH and SHvdB. Funding Acquisition: SHvdB. Guarantor: SHvdB.

Funding Oncode Base Fund to Senior Investigator S.H. van der Burg.

Competing interests None declared.

Patient consent for publication Not applicable.

Ethics approval All mouse experiments were controlled by the animal welfare committee (IvD) of the Leiden University Medical Center and approved by the national central committee of animal experiments (CCD) under the permit number AVD1160020197864, in accordance with the Dutch Act on Animal Experimentation and EU Directive 2010/63/EU.

Provenance and peer review Not commissioned; externally peer reviewed.

Data availability statement Data are available on reasonable request. Further information and requests for resources and reagents should be directed to the lead contact SHvdB (shvdberg@lumc.nl).

Supplemental material This content has been supplied by the author(s). It has not been vetted by BMJ Publishing Group Limited (BMJ) and may not have been peer-reviewed. Any opinions or recommendations discussed are solely those of the author(s) and are not endorsed by BMJ. BMJ disclaims all liability and responsibility arising from any reliance placed on the content. Where the content includes any translated material, BMJ does not warrant the accuracy and reliability of the translations (including but not limited to local regulations, clinical guidelines, terminology, drug names and drug dosages), and is not responsible for any error and/or omissions arising from translation and adaptation or otherwise.

Open access This is an open access article distributed in accordance with the Creative Commons Attribution Non Commercial (CC BY-NC 4.0) license, which permits others to distribute, remix, adapt, build upon this work non-commercially, and license their derivative works on different terms, provided the original work is

properly cited, appropriate credit is given, any changes made indicated, and the use is non-commercial. See <http://creativecommons.org/licenses/by-nc/4.0/>.

ORCID iDs

Marit J van Elsas <http://orcid.org/0000-0001-9955-6356>
 Anders Etzerodt <http://orcid.org/0000-0002-6757-2068>
 Thorbald Van Hall <http://orcid.org/0000-0002-9115-558X>
 Sjoerd H van der Burg <http://orcid.org/0000-0002-6556-0354>

REFERENCES

- 1 Massarelli E, William W, Johnson F, *et al.* Combining immune checkpoint blockade and tumor-specific vaccine for patients with incurable human papillomavirus 16-related cancer: a phase 2 clinical trial. *JAMA Oncol* 2019;5:67–73.
- 2 Brahmer J, Reckamp KL, Baas P, *et al.* Nivolumab versus docetaxel in advanced squamous-cell non-small-cell lung cancer. *N Engl J Med* 2015;373:123–35.
- 3 van Elsas MJ, van Hall T, van der Burg SH. Future challenges in cancer resistance to immunotherapy. *Cancers (Basel)* 2020;12:935.
- 4 Saleh R, Elkord E. Treg-mediated acquired resistance to immune checkpoint inhibitors. *Cancer Lett* 2019;457:168–79.
- 5 Meyer C, Cagnon L, Costa-Nunes CM, *et al.* Frequencies of circulating MDSC correlate with clinical outcome of melanoma patients treated with ipilimumab. *Cancer Immunol Immunother* 2014;63:247–57.
- 6 Zaretsky JM, Garcia-Diaz A, Shin DS, *et al.* Mutations associated with acquired resistance to PD-1 blockade in melanoma. *N Engl J Med* 2016;375:819–29.
- 7 Sade-Feldman M, Jiao YJ, Chen JH, *et al.* Resistance to checkpoint blockade therapy through inactivation of antigen presentation. *Nat Commun* 2017;8:1136.
- 8 Chen S, Lee L-F, Fisher TS, *et al.* Combination of 4-1BB agonist and PD-1 antagonist promotes antitumor effector/memory CD8 T cells in a poorly immunogenic tumor model. *Cancer Immunol Res* 2015;3:149–60.
- 9 Demaria S, Kawashima N, Yang AM, *et al.* Immune-mediated inhibition of metastases after treatment with local radiation and CTLA-4 blockade in a mouse model of breast cancer. *Clin Cancer Res* 2005;11:728–34.

- 10 Curran MA, Montalvo W, Yagita H, *et al.* PD-1 and CTLA-4 combination blockade expands infiltrating T cells and reduces regulatory T and myeloid cells within B16 melanoma tumors. *Proc Natl Acad Sci U S A* 2010;107:4275–80.
- 11 Beyranvand Nejad E, Labrie C, Abdulrahman Z, *et al.* Lack of myeloid cell infiltration as an acquired resistance strategy to immunotherapy. *J Immunother Cancer* 2020;8:e001326.
- 12 Hamann D, Baars PA, Rep MH, *et al.* Phenotypic and functional separation of memory and effector human CD8+ T cells. *J Exp Med* 1997;186:1407–18.
- 13 van Montfoort N, Borst L, Korner MJ, *et al.* Nkg2A blockade potentiates CD8 T cell immunity induced by cancer vaccines. *Cell* 2018;175:1744–1755.
- 14 Etzerodt A, Tsalkitzi K, Maniecki M, *et al.* Specific targeting of CD163+ TAMs mobilizes inflammatory monocytes and promotes T cell-mediated tumor regression. *J Exp Med* 2019;216:2394–411.
- 15 Etzerodt A, Maniecki MB, Graversen JH, *et al.* Efficient intracellular drug-targeting of macrophages using stealth liposomes directed to the hemoglobin scavenger receptor CD163. *J Control Release* 2012;160:72–80.
- 16 Jablonski KA, Amici SA, Webb LM, *et al.* Novel markers to delineate murine M1 and M2 macrophages. *PLoS One* 2015;10:e0145342.
- 17 Liu M, Tong Z, Ding C, *et al.* Transcription factor c-maf is a checkpoint that programs macrophages in lung cancer. *J Clin Invest* 2020;130:2081–96.
- 18 Barros MHM, Hauck F, Dreyer JH, *et al.* Macrophage polarisation: an immunohistochemical approach for identifying M1 and M2 macrophages. *PLoS One* 2013;8:e80908.
- 19 Santegoets SJ, Duurland CL, Jordanova EJ, *et al.* Cd163+ cytokine-producing cdc2 stimulate intratumoral type 1 T cell responses in HPV16-induced oropharyngeal cancer. *J Immunother Cancer* 2020;8:e001053.
- 20 Supek F, Bošnjak M, Škunca N, *et al.* REVIGO summarizes and visualizes long lists of gene ontology terms. *PLoS One* 2011;6:e21800.
- 21 Fantin A, Vieira JM, Gestri G, *et al.* Tissue macrophages act as cellular chaperones for vascular anastomosis downstream of VEGF-mediated endothelial tip cell induction. *Blood* 2010;116:829–40.
- 22 DeLisser HM, Newman PJ, Albelda SM. Molecular and functional aspects of PECAM-1/CD31. *Immunol Today* 1994;15:490–5.
- 23 Lee GR, Shaefi S, Otterbein LE. Ho-1 and CD39: it takes two to protect the realm. *Front Immunol* 2019;10:1765.
- 24 Maines MD. The heme oxygenase system: a regulator of second messenger gases. *Annu Rev Pharmacol Toxicol* 1997;37:517–54.
- 25 Etzerodt A, Moulin M, Doktor TK, *et al.* Tissue-Resident macrophages in omentum promote metastatic spread of ovarian cancer. *J Exp Med* 2020;217:e20191869.
- 26 Sharma AA *et al.* Onco-fetal reprogramming of endothelial cells drives immunosuppressive macrophages in hepatocellular carcinoma in brief onco-fetal reprogramming of endothelial cells drives immunosuppressive macrophages in hepatocellular carcinoma. *Cell* 2020;183:377–94.
- 27 Casanova-Acebes M, Dalla E, Leader AM, *et al.* Tissue-Resident macrophages provide a pro-tumorigenic niche to early NSCLC cells. *Nature* 2021;595:578–84.
- 28 Gusak A, Fedorova L, Lepik K, *et al.* Immunosuppressive microenvironment and efficacy of PD-1 inhibitors in relapsed/refractory classic Hodgkin lymphoma: checkpoint molecules landscape and macrophage populations. *Cancers (Basel)* 2021;13:5676.
- 29 Larroquette M, Guegan J-P, Besse B, *et al.* Spatial transcriptomics of macrophage infiltration in non-small cell lung cancer reveals determinants of sensitivity and resistance to anti-PD1/PD-L1 antibodies. *J Immunother Cancer* 2022;10:e003890.
- 30 DeNardo DG, Ruffell B. Macrophages as regulators of tumour immunity and immunotherapy. *Nat Rev Immunol* 2019;19:369–82.
- 31 Loyher P-L, Hamon P, Laviron M, *et al.* Macrophages of distinct origins contribute to tumor development in the lung. *J Exp Med* 2018;215:2536–53.
- 32 Zhu Y, Herndon JM, Sojka DK, *et al.* Tissue-resident macrophages in pancreatic ductal adenocarcinoma originate from embryonic hematopoiesis and promote tumor progression. *Immunity* 2017;47:323–38.
- 33 Gibbings SL, Goyal R, Desch AN, *et al.* Transcriptome analysis highlights the conserved difference between embryonic and postnatal-derived alveolar macrophages. *Blood* 2015;126:1357–66.
- 34 Chow A, Schad S, Green MD, *et al.* Tim-4+ cavity-resident macrophages impair anti-tumor CD8+ T cell immunity. *Cancer Cell* 2021;39:973–988.
- 35 Alaluf E, Vokaer B, Detavernier A, *et al.* Heme oxygenase-1 orchestrates the immunosuppressive program of tumor-associated macrophages. *JCI Insight* 2020;5:e133929.
- 36 Petrillo M, Zannoni GF, Martinelli E, *et al.* Polarisation of tumor-associated macrophages toward M2 phenotype correlates with poor response to chemoradiation and reduced survival in patients with locally advanced cervical cancer. *PLoS One* 2015;10:e0136654.
- 37 Tomiyama H, Matsuda T, Takiguchi M. Differentiation of human CD8 (+) T cells from a memory to memory/effector phenotype. *J Immunol* 2002;168:5538–50.
- 38 Peske JD, Thompson ED, Gemta L, *et al.* Effector lymphocyte-induced lymph node-like vasculature enables naive T-cell entry into tumours and enhanced anti-tumour immunity. *Nat Commun* 2015;6:1–15.
- 39 Thompson ED, Enriquez HL, Fu Y-X, *et al.* Tumor masses support naive T cell infiltration, activation, and differentiation into effectors. *J Exp Med* 2010;207:1791–804.
- 40 Yu P, Lee Y, Liu W, *et al.* Priming of naive T cells inside tumors leads to eradication of established tumors. *Nat Immunol* 2004;5:141–9.
- 41 Ensan S, Li A, Besla R, *et al.* Self-Renewing resident arterial macrophages arise from embryonic CX3CR1 (+) precursors and circulating monocytes immediately after birth. *Nat Immunol* 2016;17:159–68.
- 42 Pinto AR, Paolicelli R, Salimova E, *et al.* An abundant tissue macrophage population in the adult murine heart with a distinct alternatively-activated macrophage profile. *PLoS One* 2012;7:e36814.
- 43 Riabov V, Gudima A, Wang N, *et al.* Role of tumor associated macrophages in tumor angiogenesis and lymphangiogenesis. *Front Physiol* 2014;5:75.
- 44 Chakarov S, Lim HY, Tan L, *et al.* Two distinct interstitial macrophage populations coexist across tissues in specific subtissular niches. *Science* 2019;363.
- 45 O'Rourke SA, Dunne A, Monaghan MG. The role of macrophages in the infarcted myocardium: orchestrators of ECM remodeling. *Front Cardiovasc Med* 2019;6:101.
- 46 Winkler J, Abisoye-Ogunniyan A, Metcalf KJ, *et al.* Concepts of extracellular matrix remodelling in tumour progression and metastasis. *Nat Commun* 2020;11:5120.
- 47 Di Martino JS, Akhter T, Bravo-Cordero JJ. Remodeling the ECM: implications for metastasis and tumor dormancy. *Cancers (Basel)* 2021;13:4916.
- 48 Giussani M, Triulzi T, Sozzi G, *et al.* Tumor extracellular matrix remodeling: new perspectives as a circulating tool in the diagnosis and prognosis of solid tumors. *Cells* 2019;8:81.
- 49 Krzyszczyk P, Schloss R, Palmer A, *et al.* The role of macrophages in acute and chronic wound healing and interventions to promote pro-wound healing phenotypes. *Front Physiol* 2018;9:419.
- 50 Ferreira DW, Ulecia-Morón C, Alvarado-Vázquez PA, *et al.* Cd163 overexpression using a macrophage-directed gene therapy approach improves wound healing in ex vivo and in vivo human skin models. *Immunobiology* 2020;225.
- 51 Hughes R, Qian B-Z, Rowan C, *et al.* Perivascular M2 macrophages stimulate tumor relapse after chemotherapy. *Cancer Res* 2015;75:3479–91.
- 52 Arnold JN, Magiera L, Kraman M, *et al.* Tumoral immune suppression by macrophages expressing fibroblast activation protein- α and heme oxygenase-1. *Cancer Immunol Res* 2014;2:121–6.
- 53 Luu Hoang KN, Anstee JE, Arnold JN. The diverse roles of heme oxygenase-1 in tumor progression. *Front Immunol* 2021;12:658315.
- 54 Muliaditan T, Opzoomer JW, Caron J, *et al.* Repurposing tin mesoporphyrin as an immune checkpoint inhibitor shows therapeutic efficacy in preclinical models of cancer. *Clin Cancer Res* 2018;24:1617–28.
- 55 Ahmad IM, Dafferner AJ, O'Connell KA, *et al.* Heme oxygenase-1 inhibition potentiates the effects of nab-paclitaxel-gemcitabine and modulates the tumor microenvironment in pancreatic ductal adenocarcinoma. *Cancers (Basel)* 2021;13:2264.
- 56 Hirai K, Sasahira T, Ohmori H, *et al.* Inhibition of heme oxygenase-1 by zinc protoporphyrin IX reduces tumor growth of LL/2 lung cancer in C57BL mice. *Int J Cancer* 2007;120:500–5.
- 57 Zhang Z, Liu S, Zhang B, *et al.* T cell dysfunction and exhaustion in cancer. *Front Cell Dev Biol* 2020;8:17.
- 58 Zhang Q, Liu L, Gong C, *et al.* Prognostic significance of tumor-associated macrophages in solid tumor: a meta-analysis of the literature. *PLoS One* 2012;7:e50946.
- 59 Cotechini T, Atallah A, Grossman A. Tissue-Resident and recruited macrophages in primary tumor and metastatic microenvironments: potential targets in cancer therapy. *Cells* 2021;10:960.
- 60 Strachan DC, Ruffell B, Oei Y, *et al.* Csf1R inhibition delays cervical and mammary tumor growth in murine models by attenuating the

- turnover of tumor-associated macrophages and enhancing infiltration by CD8+ T cells. *Oncoimmunology* 2013;2:e26968.
- 61 Zhu Y, Knolhoff BL, Meyer MA, *et al.* CSF1/CSF1R blockade reprograms tumor-infiltrating macrophages and improves response to T-cell checkpoint immunotherapy in pancreatic cancer models. *Cancer Res* 2014;74:5057–69.
- 62 Sluijter M, van der Sluis TC, van der Velden PA, *et al.* Inhibition of CSF-1R supports T-cell mediated melanoma therapy. *PLoS One* 2014;9:e104230.
- 63 Ries CH, Cannarile MA, Hoves S, *et al.* Targeting tumor-associated macrophages with anti-CSF-1R antibody reveals a strategy for cancer therapy. *Cancer Cell* 2014;25:846–59.
- 64 Ordentlich P. Clinical evaluation of colony-stimulating factor 1 receptor inhibitors. *Semin Immunol* 2021;54:101514.
- 65 van der Sluis TC, Sluijter M, van Duikerken S, *et al.* Therapeutic peptide vaccine-induced CD8 T cells strongly modulate intratumoral macrophages required for tumor regression. *Cancer Immunol Res* 2015;3:1042–51.
- 66 Thoreau M, Penny HL, Tan K, *et al.* Vaccine-induced tumor regression requires a dynamic cooperation between T cells and myeloid cells at the tumor site. *Oncotarget* 2015;6:27832–46.
- 67 Feng M, Jiang W, Kim BYS, *et al.* Phagocytosis checkpoints as new targets for cancer immunotherapy. *Nat Rev Cancer* 2019;19:568–86.
- 68 Theruvath *et al.* Anti-GD2 synergizes with CD47 blockade to mediate tumor eradication. *Nature* 2022.
- 69 Logtenberg MEW, Jansen JHM, Raaben M, *et al.* Glutaminy l cyclase is an enzymatic modifier of the CD47- SIRP α axis and a target for cancer immunotherapy. *Nat Med* 2019;25:612–9.
- 70 Yang C, Wei C, Wang S, *et al.* Elevated CD163+/CD68+ ratio at tumor invasive front is closely associated with aggressive phenotype and poor prognosis in colorectal cancer. *Int J Biol Sci* 2019;15:984–98.
- 71 Lima L, Oliveira D, Tavares A, *et al.* The predominance of M2-polarized macrophages in the stroma of low-hypoxic bladder tumors is associated with BCG immunotherapy failure. *Urol Oncol* 2014;32:449–57.
- 72 Berry S, Giraldo NA, Green BF, *et al.* Analysis of multispectral imaging with the astropath platform informs efficacy of PD-1 blockade. *Science* 2021;372:372.
- 73 Lin KY, Guarneri FG, Staveley-O'Carroll KF, *et al.* Treatment of established tumors with a novel vaccine that enhances major histocompatibility class II presentation of tumor antigen. *Cancer Res* 1996;56:21–6.
- 74 Lee JW, Komar CA, Bengsch F, *et al.* Genetically engineered mouse models of pancreatic cancer: the KPC model (LSL-kras(g12d/+);LSL-trp53(r172h/+);pdx-1-cre), its variants, and their application in immuno-oncology drug discovery. *Curr Protoc Pharmacol* 2016;73:14.
- 75 Belkina AC, Ciccolella CO, Anno R, *et al.* Automated optimized parameters for T-distributed stochastic neighbor embedding improve visualization and analysis of large datasets. *Nat Commun* 2019;10:1–12.
- 76 Lau SP, van Montfoort N, Kinderman P, *et al.* Dendritic cell vaccination and CD40-agonist combination therapy licenses T cell-dependent antitumor immunity in a pancreatic carcinoma murine model. *J Immunother Cancer* 2020;8:e000772.